Physical Model Comparison of Gray and Green Mitigation

Alternatives for Flooding and Wave Force Reduction in an

3 Idealized Urban Coastal Environment

4

1

2

- 5 Hai Van Dang
- 6 Ph.D. Candidate, Department of Marine Science and Convergent Engineering, Hanyang University
- 7 ERICA, Ansan, Republic of Korea. Email: dangvanhai@hanyang.ac.kr.
- 8 Hyoungsu Park
- 9 Assistant Professor, Department of Civil and Environmental Engineering, College of Engineering,
- 10 University of Hawaii at Mānoa, Email: hpark9@hawaii.edu.
- 11 Sungwon Shin*
- 12 Professor, Department of Marine Science and Convergent Engineering, Hanyang University ERICA,
- 13 Ansan, Republic of Korea, Email: <u>sungwshin@hanyang.ac.kr</u>, Tel: 031–400–5533.
- 14 Tori Tomiczek
- 15 Associate Professor, United States Naval Academy, 590 Holloway Road, Mail Stop 11D, Annapolis,
- 16 MD, 21402, USA, Email: vjohnson@usna.edu.
- 17 Daniel T. Cox
- 18 Professor, School of Civil and Construction Engineering, Oregon State University, Corvallis, OR
- 19 97331–2302, USA, Email: dan.cox@oregonstate.edu.
- 20 Eunju Lee
- 21 Ph.D. Student, Department of Marine Science and Convergent Engineering, Hanyang University
- 22 ERICA, Ansan, Republic of Korea, Email: ejulee@hanyang.ac.kr.
- 23 Dayeon Lee
- 24 M.S, Department of Marine Science and Convergent Engineering, Hanyang University ERICA,
- 25 Ansan, Republic of Korea, Email: dyl12638@gmail.com.
- 26 Pedro Lomonaco
- 27 Director, Hinsdale Wave Research Laboratory, Oregon State University, Corvallis, OR 97331–2302,
- 28 USA, Email: pedro.lomonaco@oregonstate.edu.
- 29 * Corresponding Author

Abstract

31 32 33

34

35

36

37

38

39

40

41

42

43

44

45

46

47

48

49

50

51

52

53

A 1:16 scaled physical model was constructed to investigate the effectiveness of a seawall, a submerged breakwater, and mangrove forests to mitigate overland flooding and forces on structures in an idealized urban coastal environment. The experiment was performed using tsunami-like waves at different water levels, wave amplitudes, and time scales to simulate long-wave dynamics. The baseline condition (no mitigation), seawall, submerged breakwater, and mangrove forest were tested individually, and the seawall and submerged breakwater were also tested in combination. Wave gauges, acoustic Doppler velocimeters, loadcells, and pressure gauges were used to measure wave elevations, velocities, forces, and pressures on coastal structures, respectively. The performance of these hard structures and mangroves was compared through their effects on wave elevation, particle velocity, and force reduction. Experimental results showed that each protecting structure reduced the horizontal wave forces and inland flow hydrodynamics in the low-water-level case, with a similar performance by the individual seawall, submerged breakwater, and four rows of mangroves. The combined configuration, when the seawall and submerged breakwater were installed simultaneously, caused the most significant maximum force percent reduction by approximately 50%, while mangrove forests arranged in eight rows resulted in a force reduction of 46% in the first building array. However, in the high-water-level cases, the impulsive force measured with the presence of the submerged breakwater was larger than in the baseline case; thus, the submerged breakwater may amplify the impulsive force on the vertical building rows for certain incident wave conditions. Generally, the combined hard structures induced the lowest force reduction factor measured in almost every building row compared to the seawall, submerged breakwater, and mangroves considered separately for all wave conditions and water levels. That means this multi-tiered configuration showed better performance than individual alternatives in reducing horizontal forces inland than the individual alternatives considered separately.

54 55

Keywords: Overland flow, Submerged breakwater, Seawall, Mangroves, Force mitigation.

565758

1. Introduction

59 60

61

62

63

64

65

66

67

68

Several urbanized low-lying coastal communities are vulnerable to flooding events generated by high surge levels and extreme waves (Sogut et al., 2020). Currently, the frequency of inundation events is growing dramatically with increasing intensities due to the sea level rise driven by climate change (Sweet et al., 2022). Church et al. (2013) suggested global mean sea levels are expected to increase from 0.52 m to 0.98 m by 2100, placing near-coast communities at risk, especially those lowlands located under storm tide levels. An additional significant contributor to coastal flooding originates from the extreme wave induced by hazardous events such as storms and tsunamis. Increasing the degree of overflow impacts coupled with growing population densities requires more protective strategies to mitigate the effects of natural hazards and improve coastal resilience (Chang and Mori, 2021).

1.1. Overland flows on coastal communities

Tsunami-induced overland flows are likely to seriously damage coastal infrastructures and result in excessive loss of life. The last few decades have experienced several significant tsunami events, such as the Indian Ocean tsunami in 2004 (e.g., Koshimura et al., 2009), the Samoan tsunami in 2009 (e.g., Okal et al., 2010), the Chile tsunami in 2010 (e.g., Esteban et al., 2013), and the Tohoku tsunami in 2011 (e.g., Mimura et al., 2011). In particular, the Tohoku earthquake ($M_w = 9$) generated a tsunami with an inundation depth of approximately 17 m at certain places near the shorelines, damaging numerous inland buildings and causing around 18,550 fatalities or missing people (Heller, 2019).

Hurricanes can pose a significant threat to coastal buildings and infrastructures. Four of the top five costliest hurricanes in the United States occurred between 2012 and 2017 after accounting for inflation to 2017 dollars: Hurricane Harvey in 2017 (e.g., Aghabaei et al., 2018), Hurricane Sandy in 2012 (e.g., Sopkin et al., 2014), and Hurricanes Maria and Irma in 2017 (e.g., Cox et al., 2019) (National Oceanic and Atmospheric Administration (NOAA) and National Hurricane Center (NHC), 2018). Hurricane Katrina, the costliest hurricane in the United States, made landfall in Florida, Louisiana, and Mississippi in 2005 and caused 160 billion dollars in damages (NOAA and NHC, 2018). Eamon et al. (2007) indicated that over 133 thousand houses were destroyed or severely damaged, and approximately 250 deaths were witnessed in only the Mississippi coastal area during this event.

Extreme overland flows could have extensive impacts on coastal communities because the existing defensive structures may be insufficient to protect near-coast areas (Mori and Takahashi, 2012), particularly as coastal population densities continue to increase along with exposure to sea-level rise and coastal flooding hazards (Neumann et al., 2015). Therefore, evaluating the effectiveness of flood mitigation structures for coastal areas is of great importance. Some typical types of shielding structures against overland flows are studied, including conventional, "gray" structures such as seawalls (e.g., Kihara et al., 2015; Thomas and Cox, 2012), eco-friendly structures such as submerged breakwaters (e.g., Wu and Hsiao, 2013; Shin et al., 2019), and natural, "green" protection countermeasures such as coastal mangroves (e.g., Chang and Mori, 2021; Bridges et al., 2021; Tomiczek et al., 2020a). Although the role of these mitigation structures has been recognized in attenuating long wave propagation, thorough quantification of flow hydrodynamic and force reduction in coastal communities protected by these mitigation structures is limited, causing several uncertainties in the comparative performance among mitigation alternatives. These uncertainties can result in challenges in the broad application of protection measures.

 $\begin{array}{c} 102 \\ 103 \end{array}$

1.2. Previous studies of mitigation measures

105 1.2.1. Seawalls

Seawalls have been widely constructed to defend coastal cities worldwide from coastal flooding. Lukkunaprasit and Ruangrassamee (2008) conducted field observations after the 2004 tsunami in Thailand and highlighted that coastal retaining walls (seawalls) with a height of 1 m reduced tsunamigenerated damages to subsequent buildings compared to those without any protection. In addition, several scientific studies have been carried out to investigate the performance of seawalls against tsunami-like and storm-wave impacts. Cross (1967) performed a pioneering small-scale experiment on tsunami pressures on vertical seawalls. In the study, an empirical equation was proposed considering momentum and hydrostatic terms to calculate maximum pressures at the base of a seawall. Ramsden (1996) carried out small-scale tests to develop a tsunami force equation by replacing these momentum terms with the bore velocity, wave run-up, and bore-height-and-inundation-depth ratio. This equation is more easily applied compared to the equation of Cross (1967) because local bore heights and inundation depths are more readily available than inundation velocities in the tsunami field reconnaissance. More recently, Oshnack et al. (2009) conducted a scaled experiment to examine the effects of a small onshore seawall with six different heights in reducing forces caused by tsunami bores on a rigid wall. Thomas and Cox (2012) extended the study by systematically varying the locations and heights of a seawall to investigate the influence of a finite-length seawall in mitigating tsunami loadings on buildings. This study indicated that the percentages of maximum and average force reductions for the seawall cases ranged from 0% (no reduction) to 90% relative to baseline conditions (no seawall). Two empirical equations were suggested to estimate maximum and average force reduction factors as a function of the offshore bore heights, seawall heights, and the relative positions of the seawall between the design building and shorelines (Thomas and Cox, 2012). Rahman et al. (2014) performed a smallscale experiment to quantify tsunami forces on onshore buildings defended by a seawall with different types, heights, and positions. Results showed that higher seawalls located closer to buildings resulted in a maximum force reduction of 41%; however, the maximum force reduction was 27% when the seawall height was reduced by half (Rahman et al., 2014). Several advanced studies (e.g., Eurotop, 2018) have been performed to assess the design of structures to minimize run-up and overtopping on seawalls during storm impacts. However, those studies only investigated the efficiency of seawalls against wave impacts or overtopping on a single structure. The influence of seawalls on force reduction and flow transformation in a series of building arrays, similar to most real-world coastal communities, is less understood.

136137138

107

108

109

110

111

112

113

114

115

116

117

118

119

120

121

122

123

124

125

126

127

128

129

130

131

132

133

134

135

1.2.2. Submerged Breakwaters

139

140

141

142

143

Jeffreys (1944) proposed pioneering studies on wave transmission above a rectangular submerged breakwater, followed by several other studies on wave-breakwater interaction (e.g., Kobayashi and Wurjanto, 1989; Twu et al., 2001). Recently, Ting et al. (2004) used hydraulic tests to examine the influence of submerged breakwaters with eight geometries and porosities from 0.421 to 0.912 on non-

144

145

146

147

148

149

150

151

152

153

154

155

156

157

158

159

160

161

162

163

164

165

166

167

168

169

170

171

172

173

174

175

176

177

178

179

180

breaking wave transformation. Cokgor and Kapdasli (2005) conducted an experimental study to determine wave transmission coefficient values in a submerged breakwater with different shapes. The study analyzed the effects of porosities between 0.57 and 0.34 and crest-height-to-water-depth ratios ranging from 0.83 to 1.00. Moreover, Shin et al. (2019) carried out a two-dimensional hydraulic test to examine the influences of the relative crest height, crest width, wave steepness, and permeability of an artificial reef (a kind of low-crested breakwater) on wave dissipation. An empirical formula based on these parameters was proposed to estimate wave transmission coefficients for a wide range of submerged breakwaters.

In the case of submerged breakwaters under tsunami conditions, Silva et al. (2000) investigated porous submerged breakwater effects on the reflection and transmission of solitary waves by physical and theoretical methods using the inverse Fourier transform. Irtem et al. (2011; 2012) conducted a series of physical model experiments to compare the influence of the permeable and impermeable submerged breakwaters on tsunami run-up heights. Regarding the numerical investigation, Ha et al. (2014) proposed a three-dimensional Large Eddy Simulation (LES) numerical model to predict tsunami runup heights around the submerged breakwater in the surf zone and investigate wave reflection, transmission, and dissipation coefficients. This study showed that submerged breakwaters with an appropriate design could reduce tsunami transmission. Sun et al., 2020 numerically investigated the effectiveness of an idealized submerged breakwater in reducing solitary wave-induced hydrodynamic forces on coastal bridge decks through varying wave conditions and structural parameters, including spacing distances, permeability, and height-width-ratios of the submerged breakwater. This result indicated installation of the submerged breakwater as a mitigation measure might reduce maximum horizontal and vertical forces on the bridge deck for most configurations. In more detail, the height of the submerged breakwater significantly affected the maximum hydrodynamic loads in the bridge deck; however, the effects of the spacing distance, permeability, and width are relatively limited (Sun et al., 2020). Most previous studies showed that submerged breakwaters might effectively reduce wave and tsunami transmission. However, Crespo et al. (2007) conducted Smooth Particle Hydrodynamic (SPH) model to investigate the performance of a dike in reducing damage to the inland vertical wall. This study reveals that increasing the dike height can decrease the force measured in the vertical wall; however, the sea dike may behave as a ramp, inducing a large overtopping jet toward the high elevation of buildings under certain circumstances. Xu et al. (2021) conducted an experiment to investigate the performance of the rectangular barrier in reducing long-wave impacts on the seawall offshore. This result indicates that when installing low barriers may cause a worse impact compared to the absence of barrier configuration. This phenomenon is also consistent with Dalrymple and Kriebel (2005) for the 2004 tsunami in Thailand, in which the tsunami flow was projected over a sloped seawall, generating an extreme run-up jet into the upper story of near-coast buildings. Moreover, the field observation reported in UNEP (2005) indicates that serious terrestrial and coastline damage was witnessed in the areas sheltered by fringing reefs, a special case of submerged structures. Thus, more thorough

investigations on the effects of submerged breakwaters on the long wave-induced inundation flow and the resulting loads on a series of inland structures are required.

183 184

1.2.3. Combination of seawalls and submerged breakwaters

185186

187

188

189

190

191

192

193

194

195

196

197

198

199

200

201

202

203

204

205

206

207

208

209

210

211

212

213214

215

216

217

As mentioned in previous studies on seawalls, increasing seawall heights could decrease horizontal forces exerted on inland structures. However, the seawall heights were designed based on aesthetic and economic feasibilities (Raby et al., 2015) and thus be lower than the unexpectedly extreme overtopping. This limitation of seawall heights may induce lower effectiveness in coastal protection during hurricane and tsunami events. The coupling effects of sea-level rise and increased frequency of flooding require improvements to existing seawalls with insufficient seawall height. Thus, guidance for retrofitting the existing structures is needed to improve coastal protection. Specifically, submerged breakwaters have been built widely to dissipate wave energy by triggering the breaking of high waves, reducing extreme wave attacks on coastal communities (Li and Zhang, 2019). Apart from wave attenuation presented in the previous subsection, submerged breakwaters have additional advantages, including their low cost and high aesthetics compared to subaerial breakwaters (Kobayashi and Wurjanto, 1989). Therefore, submerged breakwaters can be considered as a solution to support seawalls against overflows. Jeng et al. (2005) experimentally examined the interaction between incident waves, reflected waves, seawalls, submerged breakwaters, and a sandy seabed to investigate pore pressures inside the seabed foundation. Reddy et al. (2007) carried out both physical and numerical model tests to quantify the performance of different submerged breakwater configurations in reducing wave forces, wave run-up, and wave rundown on a vertical wall under regular and random waves. Neelamani and Sumalatha (2013) varied the slopes of seawalls shielded by submerged and emergent breakwaters to study the variation of wave reflection, run-up, and wave pressures on the seawall. The results indicated that wave pressures markedly decreased by 35% - 40%, and wave run-up was reduced by 50% - 60% when breakwater crest levels were equal to the still water levels. Koraim et al. (2014) investigated the hydrodynamic performance of a new type of porous seawall with a front steel screen, back solid wall, and filled rock core protected by a submerged breakwater. This configuration reduced 20% – 60% of wave run-up and less than 70% of wave reflection. Dong et al. (2020) conducted a scaled experiment to investigate the performance of different retrofitting, including a reef breakwater, recurved wall, diffraction pillars, and model vegetation supporting seawalls in attenuating wave overtopping discharges. The results showed 98% overtopping volume reduction in the recurved configurations, whereas reef breakwaters and vegetation induced reductions of 30% and 48%, respectively. Recently, Xu et al. (2021) examined tsunami forces and overturning moments on a seawall protected by a rectangular barrier. For high enough barriers, forces and overturning moments dramatically decreased compared to the absence of barrier cases. The study proposed Gaussian-typed equations to predict the reduction ratios of maximum horizontal forces and overturning moments through fractions between the barrier height and "specific

energy head" term with an R² of 0.93. The "specific energy head" containing bore velocities and water depths was used to represent the energy of stationary flows (Xu et al., 2021).

Previous studies solely investigated wave forces, pressures, and hydrodynamic characteristics on seawalls defended by submerged breakwaters rather than inundation aspects in the broader coastal environment. Therefore, understanding tsunami overflows on a series of building rows in coastal communities with the combined protection of seawall and submerged breakwater is limited.

224225

220

221

222

223

1.2.4. Green infrastructure

226227

228

229

230

231

232

233

234

235

236

237

238

239

240

241

242

243

244

245

246

247

248

249

250

251

252

253

254

Regarding the role of mangroves under coastal flooding, Marois and Mitsch (2015) indicated that mangroves could contribute to wave attenuation in direct and indirect ways. Directly, mangroves work as a series of barriers to dissipate wave turbulent kinetic energy when waves pass through the main trunk, pneumatophores, and prop root systems. Indirectly, the complex root systems of mangroves can reduce coastal soil erosion and strengthen sediment accretion, improving the stability of the coasts. Ultimately, this stability of coasts may alleviate the damages from overland flows on areas further landward (Gedan et al., 2011). However, evaluating the ability of mangroves to mitigate overland flow induced by extreme long waves is debatable and challenging (Marois and Mitsch, 2015). Taking the 2004 Indian Ocean tsunami as an example, Danielsen et al. (2005) conducted a satellite image investigation on the damage to a total of 12 villages along the southeast coast of India sheltered by mangrove forests or without any protection. The results indicated that the villages behind the dense vegetation experienced minor damage compared to those directly suffering from the tsunami attack. Their finding served as a first guideline for the potentially protective capacity of mangrove forests against tsunami overland flows. Goda et al. (2019) similarly found that mangroves protected structures and prevented damage compared to that observed for unsheltered structures during the 2018 earthquake and tsunami in Sulawesi, Indonesia. Still, Dahdoubh-Guebas and Koedam (2006) suggested some caveats in the analysis from Danielsen et al. (2005) that were not addressed. This suggestion noted that Danielsen et al. (2005) did not consider several factors impacting damage reduction, such as distance from the villages to shorelines or construction materials used for houses and other infrastructures. Kathiresan and Rajendran (2005) performed field observations in several coastal hamlets along the southeast coast of India, noting that the elevation of residential communities and distance to the shoreline highly affected the casualties and infrastructure damages. In addition, Tanaka et al. (2007) showed that geometric features of mangrove forests also influenced the capacity of wave attenuation. They found that *Rhizophora* species with a complex aerial root system were effective in reducing wave heights compared to other types of vegetation. According to several studies mentioned above, extensive research on assessing and quantifying the mangrove forests' protection capability is certainly required. While the level of mangrove protection in extreme flooding caused by tsunamis is still debatable, coastal mangroves are valuable in storm surge mitigation (Chang and Mori, 2021). Das and Vicent

(2009) investigated over 400 villages in India impacted by a supercyclone in 1999. The findings indicated that wider width between mangrove forests and the coastlines could significantly reduce the number of fatalities. Granek and Ruttenberg (2007) examined the performance of mangrove forests in experimental sites in Belize against two tropical storms, noting that mangroves provided a higher level of protection on the shorelines than those without mangroves. Moreover, Krauss et al. (2009) examined storm surge reductions by an internal mangrove marsh system and a riverine mangrove in Florida during Hurricane Charley in 2004 and Hurricane Wilma in 2005. The two hurricanes generated inundation levels of approximately 103 cm relative to the ground level; however, the site measurements showed that surge reductions of 9.4 and 4.2 cm/km were observed in the mangrove wetlands and riverine mangroves, respectively. The study implied the protective functions of mangrove forests in storm surge attenuations over large spatial scales. Based on field observations in the Florida Keys after Hurricane Irma in 2017, Tomiczek et al. (2020b) noted that waterfront structures experienced less damage when protected by red mangrove stands of moderate cross-shore width compared to waterfront structures with other shoreline treatments, indicating that for certain conditions, mangroves may be able to provide benefits at moderate spatial scales.

This field reconnaissance demonstrated the protective function of mangrove forests during tsunami waves and hurricanes. In addition, numerous scientific studies on wave attenuation and energy dissipation through mangrove forests have been conducted to better understand wave-mangrove interaction characteristics. One of the earliest models for predicting wave attenuation was proposed by the National Academy of Sciences (1977), which related wave height attenuation for linear, shallowwater waves to incident hydrodynamic conditions, vegetation geometric characteristics (e.g., stem density, height, cross-shore width), and a drag coefficient specific to the vegetation. Dalrymple et al. (1984) later extended this equation for intermediate and deep-water wave conditions, and Mendez and Losada (2004) extended the random wave model. Physical model investigations have since been performed to determine appropriate wave-vegetation interaction for a range of vegetation species (e.g., Anderson and Smith, 2014; Ozeren et al., 2014; Wu and Cox, 2015; 2016), with several focusing specifically on idealized mangrove forests (Strusińska-Correia et al., 2013; Maza et al., 2017; 2019; Chang et al., 2019; Tomiczek et al., 2020a; Kelty et al., 2022). Strusińska-Correia et al. (2013) measured wave transmission for solitary wave and tsunami bore propagation through a simplified mangrove trunk-prop root parameterization constructed at a 1:20 scale. Maza et al. (2017) constructed a 1:12-scale model of parameterized Rhizophora trunk-prop root system to measure drag coefficients and turbulent kinetic energy under unidirectional flow conditions. Maza et al. (2019) used a similarly parameterized model a 1:6 scale to investigate wave height attenuation for regular and random waves. Chang et al. (2019) determined drag and inertial coefficients for regular waves interacting with a 1:7-scale threedimensional (3D) printed model of a Rhizophora trunk and prop root system. Considering potential scale effects when determining relationships between the drag coefficient and Reynolds number using reduced-scale physical models, Kelty et al. (2022) constructed a prototype-scale physical model to

measure wave height attenuation through an 18 m idealized *Rhizophora mangle* forest. The authors found agreement between drag coefficient-Reynolds number relationships with previous reduced-scale studies when the Reynolds number was rescaled according to Froude similarity (Kelty et al., 2022).

The studies described above have provided quantified evidence for the ability of mangrove systems to attenuate wave heights, supporting several recent initiatives advocating for more widespread implementation of vegetation and other green infrastructure owing to their capacity to mitigate coastal flood hazards while providing economic, ecological, and environmental benefits (Browder et al., 2019; Bridges et al., 2021; Science for Environmental Policy, 2021; UNDRR, 2021). Few studies have examined the effects of green infrastructure in reducing loads on sheltered near-shore structures, with notable exceptions considering mangrove effects on wave load reduction for a sheltered vertical wall (Mitchell et al., 2021) and in the first row of an idealized urban array (Tomiczek et al., 2020a). Additional work is needed to understand the effects of green infrastructure throughout a coastal community and its relative performance compared to conventional gray solutions.

1.3. Study objectives

Prior to studies of tsunami inundation, small-scale experiments and field reconnaissance were taken into consideration before scaled experiments (Oshnack et al., 2009). By contrast, Oumeraci (2010) indicated that small-scale physical experiments are inappropriate in simulating wave-structure interaction due to scale effects. In addition, several physical experiments were conducted considering regular or random wave cases instead of tsunami-like waves (Oshnack et al., 2009). Thus, this study conducted a scaled experiment to provide quantitative data for tsunami loadings on inland buildings defended by a seawall, a submerged breakwater, a combined submerged breakwater-seawall system, and a moderate-scale mangrove forest. The fundamental objectives of this study include: (1) Understand the effects of a seawall, a submerged breakwater, a combined submerged breakwater-seawall system, and emergent mangroves on wave breaking and inland hydrodynamic characteristics; (2) Assess the transformation of cross-shore forces on a series of vertical building rows; (3) Quantify the shielding effects of building elements on maximum force reduction factors when long waves inundated the inland environment; (4) Compare the performance of green and gray measures in mitigating forces on coastal buildings.

Apart from section [1], this paper consists of 4 following sections as follows: Section [2] describes the wave basin, physical instruments, building specimens, wave conditions, and data processing. Section [3] presents the effects of green and gray structures on the flow depths, cross-shore velocities, and horizontal forces in the constructed environment, then discusses the performance of mangroves and gray structures in reducing horizontal forces exerted on coastal building arrays. Section [4] discusses considerations of the study regarding scale effects and suggests ideas for future work. Section [5] presents the conclusions of this study.

2. Experimental Setup

2.1. Wave basin, bathymetry, and building specimen

The physical experiment was performed in the Directional Wave Basin (DWB) of the O. H. Hinsdale Wave Research Laboratory (HWRL) at Oregon State University (Fig. 1). The DWB, equipped with a piston-type wavemaker, was 48.8 m long, 26.5 m wide, and 2.1 m deep. The coordinate system is described as follows: x and y axes denote streamwise and transverse directions, which are positive to the west and south, respectively. The origin of the x-coordinate (x = 0) is located at the neutral wavemaker position, and the y-coordinate origin (y = 0) is located at the centerline of the wave basin. The z-axis denotes the vertical direction, in which z = 0 represents the concrete basin floor, with the upward direction set as positive.

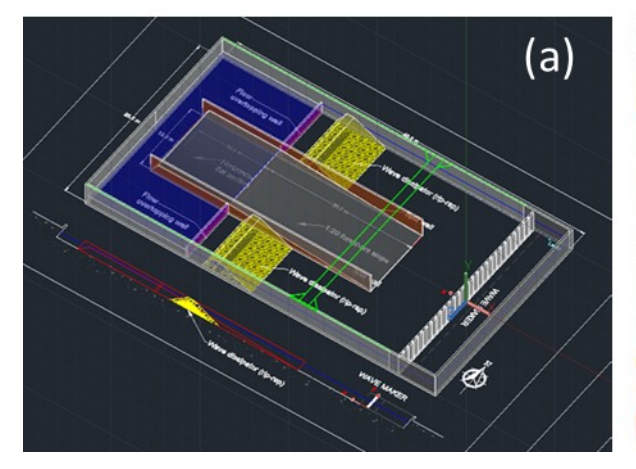




Fig. 1. (a) Graphic representation and (b) photograph of DWB physical model set-up for test bathymetry, guide walls, and water circulation system.

The bed profiles of the wave basin consist of four horizontal sections: a flat section near the wavemaker 0 m < x < 11.7 m, a 1:20 sloped section at 11.7 m < x < 31.7 m, an elevated section at 31.7 m < x < 41.7 m and a water reservoir at x > 41.7 m (Fig. 1a). At 0 m < x < 11.7 m near the wave generator, a horizontal flatbed is representative of the nearshore with a constant water depth. From x = 11.7 m onwards, the wave basin was divided into a central test platform (foreshore and coastal area with dimensions of $30 \text{ m} \times 10 \text{ m}$) and a water circulation system located north and south of the central platform. The water circulation system included a water reservoir, pumping systems, a series of split walls, and two riprap wave dissipation structures. Guide walls starting at x = 11.7 m were used to separate the central test platform from the water circulation system on either side to locate the sloping beach and coastal areas. For the water circulation system, two recirculating pumps were installed on both sides of the reservoir to provide water for the initial flatbed in the following test trials. This discharge increases the water level at the initial flatbed, creating overland flow over the whole central test platform. The overland flow discharges back to the reservoir, closing the circuit and creating a recirculation. Since the reservoir is created with two vertical walls splitting the basin across, incoming

waves will reflect and reproduce significant interference, reducing the quality of waves generated. Hence, two rubble-mound breakwaters (riprap dissipators) were installed to dissipate and reduce wave reflections. The rubble mounds also help reduce the pump discharge effects on both lateral sections (Fig. 1).

The central test platform consisted of two longitudinal sections (Fig. 2). The first section is a sloped concrete beach for 11.7 m < x < 31.7 m. This slope of 1:20 was carefully selected to allow for wave shoaling up an idealized bathymetry of a foreshore beach and flooding the coastal area during storm and tsunami events. The second section was a 10 m × 10 m horizontal flat test area with the base at an elevation of z = \pm 1.0 m relative to the basin floor, representing an urban environment for 31.7 m < x < 41.7 m. One hundred rigid building models with dimensions of 0.4 m × 0.4 m × 0.4 m were arranged in a 10 × 10 array, representing an idealized coastal city. Each building element was positioned with 0.8 m and 1.0 m (center-to-center) spacing along the x-axis and y-axis, respectively. The first building row was placed 1.6 m from the end of the slope (the shoreline to the seaward edge of the first-row building specimen). The detailed positions of the total building models can be seen in Fig. 2. Additional details of the wave basin, bathymetry, and building specimen descriptions can be found in Tomiczek et al. (2020a), Park et al. (2021), and Moris et al. (2021), which performed experiments using the similar bathymetry setup.

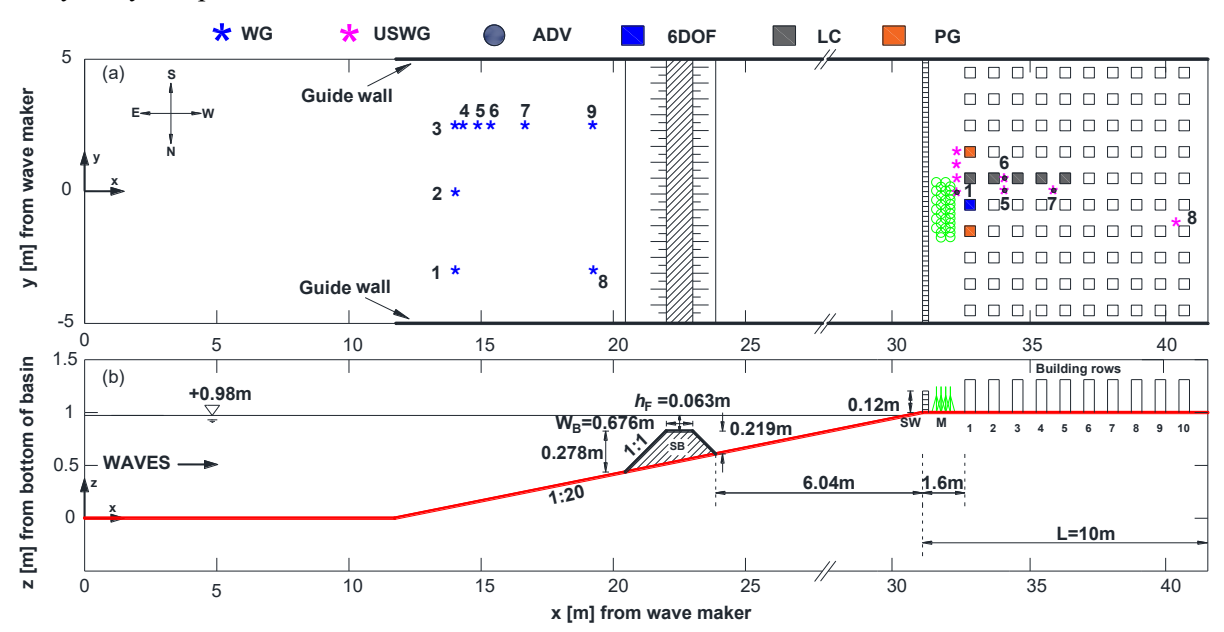


Fig. 2. (a) Plan view and (b) Cross-shore view of the main test section showing locations of seawall, submerged breakwater, and mangrove configurations, and instrumentation used: Offshore Wave Gauges (blue star); Acoustic Doppler Velocimeters (black circle); Ultrasonic Wave Gauges (magenta star); Pressure sensors (built-in two orange blocks); Submersible multi-axial loadcell (built-in blue block); Horizontal in-line loadcells (built-in five gray blocks).

2.2. Instrumentation setup

Fig. 2a presents the locations of the physical instruments used in this study, including wire resistance wave gauges (WGs), ultrasonic wave gauges (USWGs), acoustic Doppler velocimeters

(ADVs), horizontal loadcells (LCs), a six-degree-of-freedom loadcell (6DOF), and pressure gauges (PGs). Nine WGs located on the offshore slope were used to identify the incident wave characteristics and check the repeatability of waveforms, with WG2 installed close to the centerline to record the offshore free surface near the onset of the sloping section. The USWGs and ADVs were mounted on an observation and instrumentation bridge embracing the full width of the wave basin, in which ultrasonic wave gauges USWGs (1, 5, 7, and 8) were placed in the vicinity of the centerline with x-locations of 33.143 m, 34.733 m, 36.313 m, and 40.655 m relative to the wavemaker in the zeroed position, respectively. USWG6 was installed at x = 34.719 m from the second and third building row to capture the free surface displacement between the two building blocks. Four ADVs (1, 5, 6, and 7) were collocated with four USWGs (1, 5, 6, and 7) to measure the flow velocities in three directions. Moreover, eight specimens among the hundred building models were made of aluminum and were used for installing pressure sensors and loadcells. Twelve PGs were arranged in two aluminum specimens in the first building row (PG A and PG B); five loadcells (6DOF to LC6) and a 6DOF were spaced in the six remaining specimens. LCs were installed in a building model from the first to fifth building row, and a multi-axis 6DOF loadcell was located at the most seaward building model. In each PG A and PG B, six PGs were positioned along the vertical centerline of the building specimen with 0.04 m spacing (centerto-center), and the lowest PG was spaced 0.02 m above the elevated flat bottom. Photos of instrumentations used in the experiment are illustrated in Appendix A1, and detailed locations of selected instruments are specified in Table 1.

407 408

388

389

390

391

392

393

394

395

396

397

398

399

400

401

402

403

404

405

Table 1. Selected instrument locations.

Instrument Description	Instruments	x (m)	y (m)	z (m)			
Wavemaker Displacement	Wmdisp	_	0.00	_			
Wavemaker Wave Gauge	Wmwg	_	0.00	_			
Resistance Wave Gauge	WG1	14.052	-3.540	_			
Resistance Wave Gauge	WG2	14.048	-0.056	_			
Resistance Wave Gauge	WG3	14.039	2.473	_			
Resistance Wave Gauge	WG4	14.341	2.482	_			
Resistance Wave Gauge	WG6	15.394	2.474	_			
Resistance Wave Gauge	WG9	19.246	2.494	_			
Ultrasonic Wave Gauge	USWG1	33.143	0.024	2.294			
Ultrasonic Wave Gauge	USWG2	33.134	0.498	2.302			
Ultrasonic Wave Gauge	USWG4	33.180	1.992	2.305			
Ultrasonic Wave Gauge	USWG5	34.733	-0.003	2.357			
Ultrasonic Wave Gauge	USWG6	34.719	0.523	2.428			
Ultrasonic Wave Gauge	USWG7	36.313	0.037	2.376			

Ultrasonic Wave Gauge	USWG8	40.655	-1.039	1.769
Acoustic Doppler Velocimeter	ADV1	33.152	-0.019	1.020
Acoustic Doppler Velocimeter	ADV5	34.733	-0.026	1.018
Acoustic Doppler Velocimeter	ADV6	34.723	0.473	1.011
Acoustic Doppler Velocimeter	ADV7	36.304	-0.018	1.018
Six-Degree-of-Freedom Loadcell	6DOF	33.457	-0.511	1.083
Horizontal Loadcell	LC2	33.450	0.483	1.223
Horizontal Loadcell	LC3	34.229	0.474	1.223
Horizontal Loadcell	LC4	34.994	0.479	1.224
Horizontal Loadcell	LC5	35.815	0.476	1.227
Horizontal Loadcell	LC6	36.617	0.481	1.226
Pressure Gauge	PG1	33.298	-1.503	1.020
Pressure Gauge	PG2	33.367	-1.491	1.060
Pressure Gauge	PG3	33.302	-1.504	1.100
Pressure Gauge	PG4	33.279	-1.507	1.140
Pressure Gauge	PG5	33.297	-1.504	1.180
Pressure Gauge	PG6	33.327	-1.498	1.220

2.3. Mitigation options: Seawall, Submerged Breakwater and Mangrove

This experiment was a part of larger campaigns of hydrodynamic tests investigating the effects of debris advection (Park et al., 2021), progressive damage to residential structures (Duncan et al., 2021, Lee et al., 2022), mangrove vegetation (Tomiczek et al., 2020a; 2021), and macro-roughness (Moris et al., 2021). This study focuses on the effects of coastal hazard mitigation alternatives for four configurations: seawall only (SW), submerged breakwater only (SB), both seawall and submerged breakwater (SWSB), and mangroves (M) to evaluate the mitigation alternatives in comparison with the baseline conditions (without mitigation alternatives).

As an idealized physical model study, the targeting geometric scale of a submerged breakwater and seawall set as 1/16, the same as the previous mangrove experiment by Tomiczek et al., 2020a. An impermeable submerged breakwater and seawall were made of wood and spaced 7.64 m and 1.60 m relative to the first building array, respectively. The submerged breakwater was installed with a crest width (W_B) of 0.676 m and both front and back slopes of 1:1. The crest freeboard (h_F) depends on the water level. Fig. 2b shows a freeboard of 0.063 m, corresponding to a specific still water level of 0.98 m. Therefore, the crest width and freeboard of the submerged breakwater in the prototype are 11.0 m and 1.0 m, respectively. A full-length seawall was positioned on the shoreline with a crest width of 0.036 m and a height of 0.12 m, corresponding to 0.6 m and 1.9 m in the prototype scale. The details of hard structures' dimensions are illustrated in Fig. 2b.

To assess the effects of green infrastructure mitigation options, Tomiczek et al. (2020a) replaced the seawall and submerged breakwater with an idealized fringing mangrove forest. The mangroves were an idealization of a mature Rhizophora mangle (red mangrove) forest of moderate cross-shore width. The trunk-prop root models were parameterized following Ohira et al. (2013), and the spacing between trees was consistent with other field observations of mature mangrove forests, as explained in Tomiczek et al. (2020a). Two configurations were tested with cross-shore forest thicknesses of 0.51 m and 1.19 m, corresponding to four and eight rows of mangroves (4M and 8M), respectively. Rows of mangroves were staggered and comprised 13 individual mangrove specimens, with cross-shore spacing between trunks of 0.17 m (center-to-center) and an alongshore spacing between rows of 0.19 m. Each individual mangrove specimen was composed of a trunk and 22 prop roots. Polyvinyl chloride (PVC) rod with a 0.013 m diameter and 0.26 m height was used to make the main trunk, while prop roots were made of several galvanized steel wires with a diameter of 0.0025 m. The prop roots were cut to different lengths and installed by threading through 11 holes drilled in a 45° spiral pattern along the trunk, with a vertical spacing of 0.013 m and the lowest prop root installed 0.025 m above the base of the trunk. Fig. A1f (Appendix) shows the 4-row mangrove set up in front of the first building arrays. A detailed description of mangrove specimen design and construction is provided in Tomiczek et al. (2020a).

444 445 446

429

430

431

432

433

434

435

436

437

438

439

440

441

442

443

2.4. Wave Conditions

447 448

449

450

451

452

453

454

455

456

457

458

459

460

461

462

463

464

465

466

The wavemaker is driven by 30 independently programmable servo motor-driven points and 29 paddles. Each paddle has a board height of 2.0 m, a maximum stroke of 2.1 m, and a maximum velocity of 2.0 m/s, which was installed on the east side of the basin to generate waves propagating into an impermeable flat bathymetry (Tomiczek et al., 2019). The wave paddles are driven by electric actuators, and their movement was electronically controlled by computers and individually defined for each trial by users. The wavemaker can generate regular, random, transient (tsunami-like) waves, and the water circulation system installed for these experiments allowed for wave generation with and without background currents. This study only focuses on wave-induced overflows without background currents. Conventionally, solitary wave generation techniques are applied to simulate tsunami-like wave impacts on coastal structures (e.g., Goring, 1978). However, solitary waves have been acknowledged to not sufficiently represent the whole process of tsunami-induced inundation because of the large differences in tsunami wavelengths and periods between physical and prototype models (Madsen et al., 2008). In addition, Thomas and Cox (2012) showed that the solitary wave underestimates the inundation processes; thus, the tsunami-like waves presented here were generated by the error-function method, a modified solitary wave generation technique. This method used the error function time series to control wavemaker displacements to maximize inundation (Park et al., 2013; 2021). A detailed explanation of the error function technique is described by Moris et al. (2021) and Winter et al. (2020).

The whole experiment conducted a total of 51 transient (tsunami-like) wave trials, including 12 trials for SB only and SW only, 13 trials for SWSB, 6 trials for the mangrove forest, and 8 trials for the

baseline configuration (Lomonaco et al., 2020). Mitigation alternative configurations were tested for three cases with different water levels and wave parameters, including mean amplitudes and representative time scales with standard deviations, as presented in Table 2.

469470471

467

468

Table 2. Experimental tsunami-like wave conditions and water levels for all trials.

Case	Configurations	Water	Wave	Standard	Representative	Standard
		depth	amplitude	deviation	time scale	deviation
		[h](m)	[A](m)	$\left[\sigma_A\right](m)$	[T](s)	$\left[\sigma_T\right](s)$
1	Baseline; SB; SW;	0.98	0.21	0.0037	5.70	0.061
	SWSB; 4M; 8M	(dry bed)				
2	Baseline; SB;	1.1	0.14	0.0027	8.89	0.042
	SW; SWSB	(wet bed)				
3	Baseline; SB;	1.1	0.21	0.0035	5.70	0.062
	SW; SWSB	(wet bed)				

472473

474

475

476

477

478

479

480

481

482

483

484

485

486

487

488

This experiment considered two water levels of 0.98 m (Case 1) and 1.10 m (Cases 2 and 3). We refer to Case 1 as a low-water-level case and Cases 2 and 3 as high-water-level cases. Owing to time constraints, the mangrove configurations were only compared for Case 1 based on overlapping experimental conditions performed by Tomiczek et al. (2020a). In contrast, the structural countermeasures configurations were tested for all wave cases. The urban environment was elevated above 1.00 m relative to the wave basin floor, causing a series of building arrays to be located in the dry bed for the low-water-level case and submerged by 0.10 m in the high-water-level cases. Wave amplitudes were calculated based on the ensemble average of free surface elevation time series recorded at WG2 over all configurations. Standard deviations of wave amplitudes presented in Table 2 were estimated from six peak magnitudes of water surface elevations in those configurations for each wave condition. Additionally, representative time scales T_R were identified as the duration of wave signals that exceeded 10% of their amplitudes (Tomiczek et al., 2020a). Wave amplitudes increased from 0.14 m to 0.21 m, and their standard deviations (σ_A) were less than 0.0037 m. The duration of wave signals (or T_R) ranged from 5.70 s to 8.89 s, and σ_T varied from approximately 0.042 s to 0.062 s over three wave cases. Therefore, a larger incident amplitude was recorded for Cases 1 and 3, and a longer duration was generated by Case 2. A detailed time series of water surface elevations and wavemaker paddle displacements are presented in Appendix A2.

489 490 491

2.5. Data Acquisition and Processing

492 493

494

Experimental data were measured and stored using a 64-channel PXI-based real-time data acquisition system. In this study, hydrodynamic datasets were collected and processed following

methods established in previous studies (e.g., Baldock et al., 2009). Water surface elevations and cross-shore velocities were recorded at a 100 Hz sampling rate. Force and pressure data were collected at a sampling rate of 1,000 Hz, accurately measuring the magnitude of impulsive forces and pressures at the peak (e.g., Tomiczek et al., 2016). The wavemaker displacement signal was used to synchronize data collection for all instruments. The data were filtered using the lowpass filter with a cut-off frequency of 50 Hz to remove noise (Park et al., 2017). An example of data processing for the baseline configuration at wave case 2 is presented in Appendix A3. For other configurations, the data were processed in the same method.

3. Results

3.1. Effects of mitigation measures on flow depths

Fig. 3 shows the snapshots extracted from high-speed cameras at the moment of wave breaking and maximum splash-up due to wave and structure interaction for each of the three wave cases for the SW configuration. The qualitative images indicate that the seawall influences wave transformation in the inland area as the wave flows over the seawall and results in different wave-breaking characteristics for the three wave conditions. In Case 1, the wave initially broke at the slope before reaching the seawall (Fig. 3a) and impacted the buildings as a fully broken wave (Fig. 3d). However, in Case 2, for which flow depth was increased by 0.12 and the wave amplitude was decreased by 0.07 m, the wave propagated over the seawall without breaking (Fig. 3b) and directly hit the upper half of the buildings (Fig. 3e). In Case 3, the wave overtopped the seawall and broke near the first building array (Fig. 3c), immediately impacting the below part of the most seaward building row (Fig. 3f).

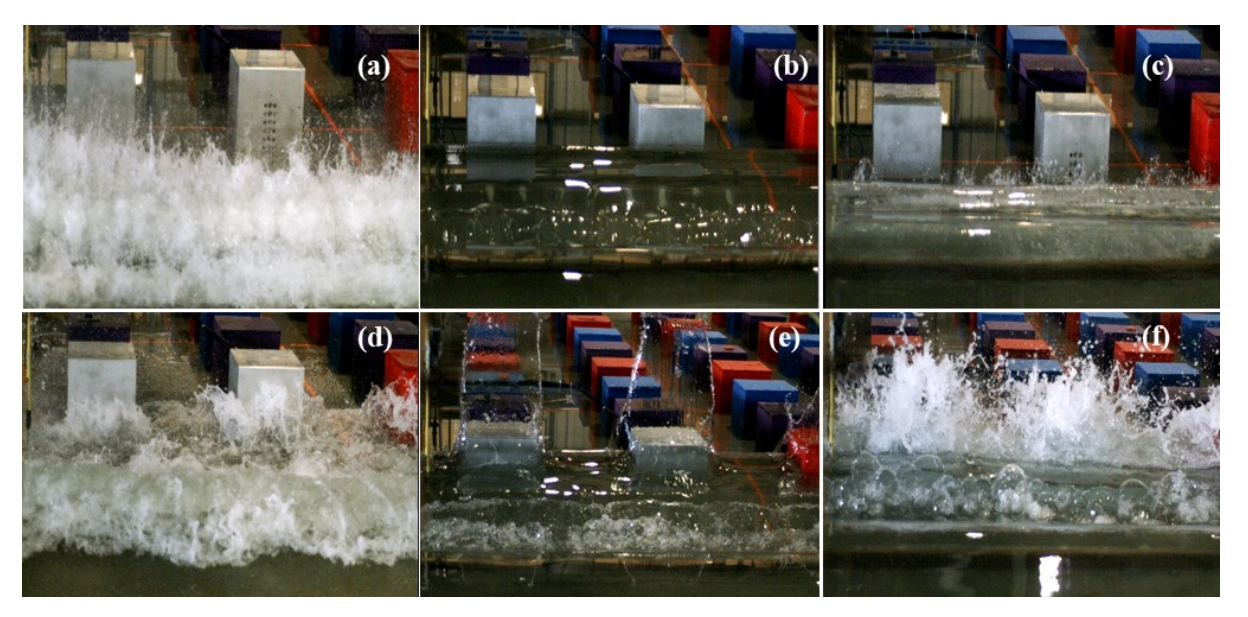


Fig. 3. Snapshots of wave breaking (upper panel) and maximum splash-up (below panel) against the beachfront buildings: (a - d) Case 1; (b - e) Case 2; (c - f) Case 3.

523

524

525

526

527

528

529

530

531

532

533

534

535

536

537

538

539

540

541

542

543

544

545

546

547

548

549

550

551

552

553

554

555

556

557

558

559

These patterns of flow propagation in the inland areas for the wave cases and varied configurations were quantitatively observed from the time histories of the flow depths measured at USWG1, which is positioned 0.1 m seaward in front of the first building row (Fig. 4). In this figure, the times series of flow depths were measured from still water level in the constructed environment for the three wave cases. Each color indicates a different configuration, with blue dashed lines, red dotted lines, magenta dash-dotted lines, green dashed lines, orange dash-dotted lines, and black solid lines indicating the SB (submerged breakwater only), SW (seawall only), SWSB (combined submerged breakwater and seawall), 4M (4 rows of mangroves), 8M (8 rows of mangroves), and baseline configurations, respectively.

For the low-water-level case of 0.98 m (Case 1), the overland flows came earlier in the baseline case than the countermeasure configurations with the arrival time at 25.36 s, 25.42 s, 25.50 s, 25.64 s, 25.85 s, and 26.05 s for the baseline, 4M, 8M, SB, SW, and SWSB configurations, respectively (Fig. 4a). Thus, all countermeasure configurations delayed the arrival time of flow propagation, while the gray structures are more effective in delaying the arrival time than the green configuration. For the presence of combined mitigation options (SWSB), the wave propagates slightly slower over shallow water due to submerged breakwater and takes a short amount of time to overtop the seawall, causing a longer arrival time than other configurations. Around 0.5 s to 0.7 s after the wave arrival times, there is a rapid jump in the flow depths. This phenomenon is because those incoming waves propagated in the urban area as bores with larger heights than the instantaneously formed surges (Moon et al., 2019). The peak flow depth measured by the baseline is larger than other countermeasure configurations for Case 1. Both the SW and SB configurations led to a flow depth of about 68% of the peak flow depth measured for the baseline condition, while mangroves in both the 4M and 8M configurations resulted in a flow depth of about 78% of that of the baseline. However, the SWSB condition (combination of the seawall and submerged breakwater) yielded a dramatic reduction of the peak flow depth to about 50% of the baseline condition. While all countermeasures resulted in a reduction in peak flow depth from the baseline condition, the mangrove configurations induced a larger peak and overall inundation depth compared to the hard structure configurations in front of the first building array. In the mangrove configurations, reflected waves from the first building row were prevented by mangrove roots, resulting in a high concentration of water particles between the first row and mangrove forests. Therefore, inundation depths measured in the mangroves are higher than those measured in hard structure configurations. Effectively, the combined seawall and submerged breakwater caused the greatest reduction in flow depths.

In Case 2, minor differences in peak elevations were observed among all structural configurations (Fig. 4b). However, in Case 3, there was a significant change over the baseline, SB, SW, and SWSB configurations (Fig. 4c). In particular, the maximum flow depths in the SB configuration were greater than those in the baseline cases for Cases 2 and 3. Particularly in Case 3, the tsunami-like wave transmitted over the submerged breakwater, inducing a hydraulic jump with a higher water elevation

than the incident wave height, which generated a stronger and steeper wave propagating toward the sloping beach. Then the wavefront with strong intensities plunged to the still water level, immediately causing vertically deflected waves that reached the high elevation of sensors and subsequently collided with the upper position of the first building row. In contrast, the presence of seawall significantly dissipated the energy of inland flow, which is attributed to the reduction of inundation depths more than in the SB configuration. Therefore, the presence of submerged breakwaters may amplify inundation levels in front of the first building row in high-water-level cases. The increased wave amplitudes by 0.07 m (from Case 2 to Case 3) or increased water levels by 0.12 m (from Case 1 to Case 3) could increase the maximum magnitudes of flow depths for three wave trials. However, changes in flow depths did not show a monotonic trend with changes in countermeasure configurations, although the SWSB case resulted in the greatest reduction of flow depths for all wave cases tested in the first building row.

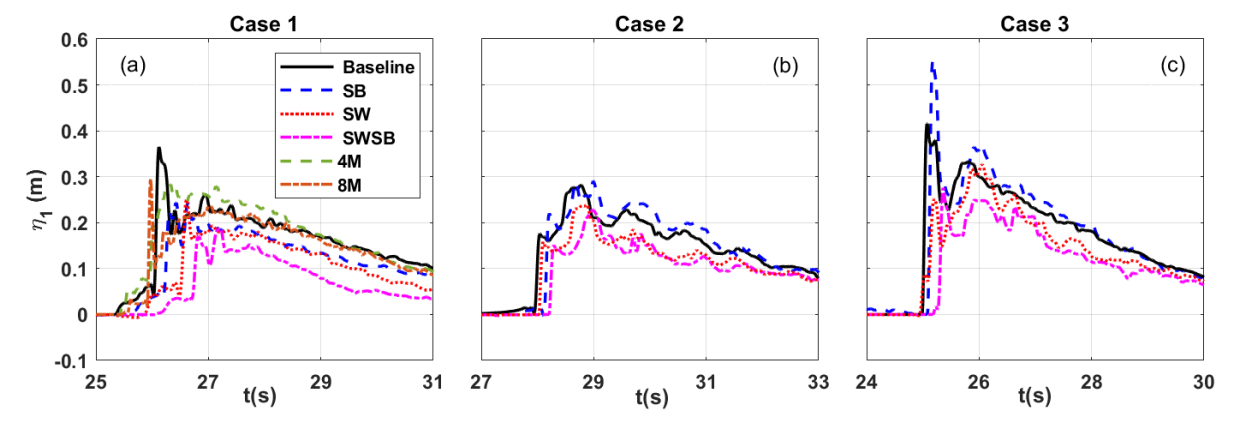


Fig. 4. Time histories of flow depths measured at USWG1 in front of the most seaward building array for three wave cases.

Fig. 5 shows the maximum flow depths from still water level versus the relative distances from shoreline X/L, where X represents the distances from the shoreline to the USWGs positions, with X=0 at the shoreline location. These distances are normalized by the total length of the elevated flat section (L=10 m) for this experimental setup. The maximum flow depths for the gray countermeasure configurations dramatically decreased from the first to third building rows (0.15 < X/L < 0.31) before gradually falling to the last array (0.31 < X/L < 1). In contrast, a slight change in the flow depth was observed in mangrove forests between 0.15 < X/L < 0.31. Generally, the decreasing trend in the maximum flow depths due to an increase in the relative distance X/L agrees with previous results from Park et al. (2013). However, in Case 3, slight local increases in flow depths at adjacent sensors at X/L = 0.31 and 0.47 (USWG5 and USWG7) in the SWSB and SB configurations were observed due to the complicated flow and structure interactions including reflection, channeling, and blocking effects over the building arrays (Kihara et al., 2021).

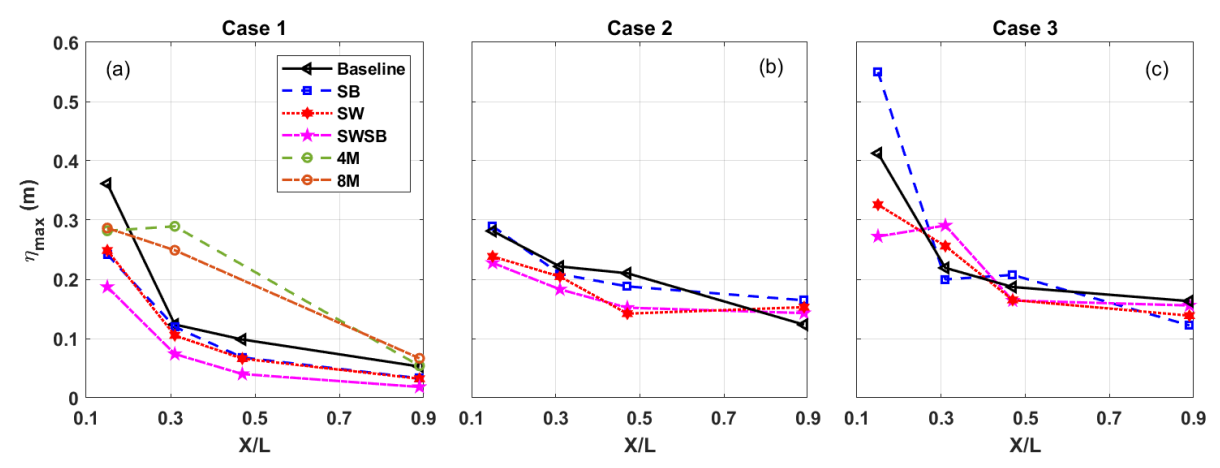


Fig. 5. Maximum flow depths measured by USWGs (1, 5, 7, and 8) as a function of the relative cross-shore distance (X/L).

To investigate the percent reduction in inundation depth, maximum onshore overland flow depths recorded by USWGs 1, 5, 7, and 8 were selected for analysis. Percent reductions were calculated considering $(\eta_c^{(i)})_{\max}$ as the maximum onshore inundation depth measured at the countermeasure configuration and $(\eta_b^{(i)})_{\max}$ as the maximum inundation depth collected from the baseline at the ultrasonic wave gauge (i) for each wave condition. Variations of flow depth percent reduction (PR) are examined by the following equation:

$$PR = \left\lceil \frac{\left(\eta_b^{(i)}\right)_{\text{max}} - \left(\eta_c^{(i)}\right)_{\text{max}}}{\left(\eta_b^{(i)}\right)_{\text{max}}} \right\rceil \times 100\%$$

$$\tag{1}$$

Table 3 shows the percent reductions in peak flow depths between countermeasure and baseline configurations at X/L = 0.15 (in front of the first building array) and the overall percent reduction for the building array. The overall percent reduction was estimated by averaging the percent reduction in water surface elevation at four USWG locations in the inland area. A positive value indicates a reduction in peak water surface elevation relative to the baseline condition.

In Case 1, the SB and SW configurations induced a similar percent reduction in peak flow depth of 32% in the first building row, and the SW configuration showed an overall percent reduction of 30%, which is slightly larger than 26% in the SB condition for the four measurement locations in the landward area. However, the combination of the submerged breakwater and seawall (SWSB) considerably reduced the baseline peak flow depths by between 50% and 53% at the first building row and landward area. The mangrove configurations caused a 22% reduction for both the 4M (4-row) and 8M (8-row) configurations relative to the baseline condition at the first building row. However, the mangrove configurations generally amplified flow depths in the landward area, with amplification of approximately 38% and 35% over the building arrays for the 4M and 8M conditions, respectively. The amplification of flow depths in the landward area may have been affected by the transient wave interaction with the vegetation and reflection owing to the mangroves and building elements (Tomiczek

et al., 2020a). The reflected waves from mangrove roots further inundated the landward area, accelerating the flow run-up on each building row, which passes through the building sides and then converges in the spacing between adjacent building rows. The convergence of flows generated an amplification of inundation depths in the landward area. However, for hard structure configurations, the reflected waves from the first building rows directly propagated offshore, which could not accelerate the landward flow; therefore, their inundation depth is considerably reduced after passing the most beachfront row.

For high-water-depth cases, maximum flow depths measured by the SB configuration were amplified by up to 33% compared to the baseline configuration in the most seaward building row. The maximum percent reduction of peak elevations for the SWSB configuration was 34%, while the SW configuration resulted in a reduction of 21%. In general, in overall wave cases tested, the SW performance for peak flow depth reduction is better than that for the SB configuration, and the SWSB configuration is the most effective countermeasure in reducing flow depths of overland tsunami-like waves in the inland area. For the low-water-depth case, the moderate-scale mangrove fringes were less effective than gray configurations in reducing peak flow depths in the inland area, although these configurations caused a measurable reduction in peak flow depths of the seaward-most row.

Table 3. Maximum percent reduction of maximum flow depths

Mitigation	Case 1		Case 2		Case 3	
Strategy	Shoreline at	Overall	Shoreline at	Overall	Shoreline at	Overall
	X/L = 0.15 (%)	(%)	X/L = 0.15 (%)	(%)	X/L = 0.15 (%)	(%)
SB	32	26	-3	-5	-33	-3
SW	32	30	15	8	34	8
SWSB	50	53	19	13	21	5
4M	22	-38	_	_	_	_
8M	22	-35	_	_	_	_

3.2. Effects of mitigation measures on cross-shore velocities

The time histories of cross-shore velocities measured at ADV1 in front of the first building row are shown in Fig. 6. For the low-water-level case of 0.98 m (Case 1), ADVs failed to capture the leading-edge velocities because ADVs were initially exposed to air, causing poor signal data for all configurations in the duration of approximately 25.36 s < t < 27.04 s until the flow depth reached its maximum (Fig. 6a). The velocity data were processed using the signal-to-noise ratios (SNR) to retain velocity signals with SNR larger than 10 dB (Kihara et al., 2015). However, Fig. 6 (b, c) shows that ADVs capture peak cross-shore velocities well for high-water-level cases (h = 1.1 m). Fig. 6 indicates that while there is a significant reduction in maximum velocities due to all countermeasures from baseline configurations in Case 1, maximum velocities are relatively similar among the baseline, SB, SW, and SWSB configurations for the high-water-depth conditions (Cases 2 and 3). Velocities

measured for the SW configurations are generally smaller than those measured for the SB configurations for the high-water-level cases.

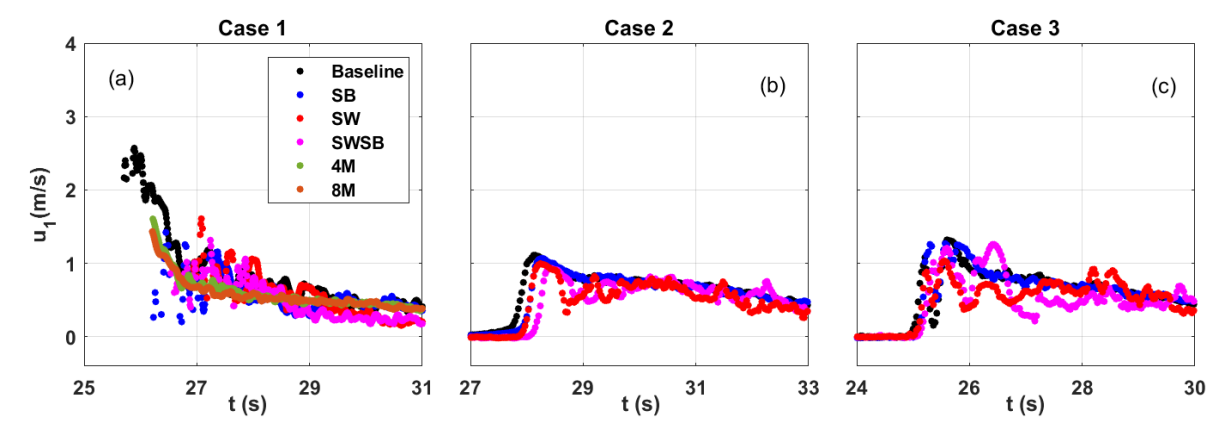


Fig. 6. Time series of cross-shore velocities measured by ADV1 for three wave cases.

Fig. 7 shows the variation of peak cross-shore velocities plotted against the relative distance from the shoreline for the *X/L* positions of three ADVs in the building array. The maximum velocities in the incident waves were calculated by averaging the single peak data value and two data values on either side of this peak. In general, cross-shore velocities increased from the first to third building array before decreasing to the last row for almost all trials. The increasing trend in cross-shore velocities is due to channeling and blocking effects. Narrow spacing between each building element may make cross-shore velocities increase in the side street (Tomiczek et al., 2016).

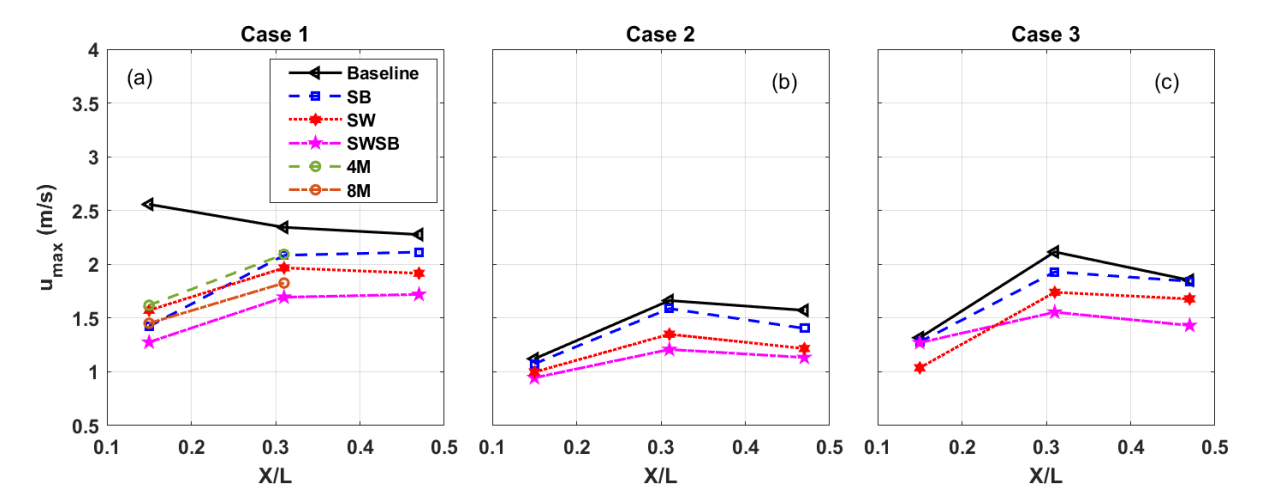


Fig. 7. Peak cross-shore velocities as a function of relative cross-shore distance (X/L).

The wet and dry conditions of the bed highly influenced the maximum cross-shore velocities recorded. While the overland flows traveled in a dry bed in Case 1, the urban array is initially partially submerged by a still water level of 0.1 m in Cases 2 and 3. In more detail, the peak velocities in the dry beds are larger than those measured in the wet beds, consistent with the previous results reported by Wüthrich et al. (2018). In wet bed conditions, strong turbulence was generated in the location where

the kinetic energy or momentum of coming bore-fronts was transferred to initial water particles located on the bottom of the landward section (St–Germain et al., 2012). This turbulence resulted in wave energy dissipation of the advancing bore fronts. Therefore, the energy dissipation could explicate the deceleration of overflow propagation in the wet beds compared to the dry beds.

The percent reduction (PR) of horizontal velocities was calculated following Equation (1) by replacing the maximum flow depths with the maximum cross-shore velocities measured in the baseline and countermeasure configurations. The SB configurations reduced horizontal velocities by 4% to 21%, and significant decreases between 11 % and 23% were observed for the SW configurations at three wave conditions. For the low-water-level case, the mangrove configurations 4M and 8M decreased the overall maximum cross-shore velocities by 20% and 30% at two ADVs in the inland area. The presence of both the seawall and submerged breakwater in the SWSB was the most effective in alleviating velocities, with an overall percent reduction of 34% over the three wave cases. Generally, the shielding structures reduced cross-shore velocities for all wave trials, and there was no large difference recorded in each mitigation configuration.

3.3. Effects of mitigation measures on horizontal forces and total impulses

The overland tsunami-like wave impacts on vertical structures experienced three stages: an initial impact phase, a reflection phase (transition phase), and a quasi-steady phase (Kihara et al., 2015; Xu et al., 2021). Forces measured in these stages are referred to as impact (impulsive forces), reflection (runup forces), and quasi-steady forces, respectively. This study presents a typical example of the wave-induced force time series on vertical buildings without any protection in Case 3 to elucidate the three stages. Fig. 8 shows the free surface elevation measured by USWG1 in front of the first building row, the horizontal force obtained by 6DOF, and the temporal variation of six hydrodynamic pressures PGs (1–6). Fig. 8c illustrates the classification of durations for three phases: an impact stage (red-shaded region), a reflection stage (blue-shaded region), and a quasi-steady stage (green-shaded region).

The leading edge of the wave arrived at the constructed specimen at 25.02 s. At that time, water elevations significantly increased, reaching a peak at 0.44 m at 25.09 s (Fig. 8a), and impulsive pressures and forces were also observed immediately in the red-shaded region (Fig. 8b, c). The rise times of six pressures to reach peak values fluctuated between 0.028 s and 0.174 s. Bullock et al. (2007) carried out large-scale experiments to investigate detailed characteristics of wave impacts on vertical walls. There are four types of impact characteristics: low- and high-aeration impacts, slightly breaking, and broken wave impacts. For low-aeration impacts, pressures were characterized by large pressure spikes and short rise times of approximately 0.08 s -0.20 s (Bullock et al., 2007). The localized pressures in the present study are similar to those in the low-aeration impacts of Bullock's study; however, the duration of pressure spikes was shorter.

From 25.19 s to 25.21 s, a "cavity phenomenon" was generated by a large amount of air entrainment between the water and vertical buildings, making pressures and forces decrease to their local minimum values. For this duration, the peak free surface elevation declined to 0.36 m. Following the impact stage, an initial reflection phase was generated (blue-shaded region), in which horizontal forces and pressures started increasing again because the cavity was filled with water particles (Fig. 8b, c). The convergence between upward and downward flows generated local high pressures and forces (Kihara et al., 2015). While incident waves in low areas continuously accelerated upward flows, the downward flows were caused by gravity effects resulting from water particles in the high position of the building element. The local peak forces of 0.46 kN were observed at 25.31 s, while the reflected water column fluctuated and collapsed to 0.23 m. From 25.70 s onwards (green-shaded region), the forces and pressures were relatively equal to the hydrostatic forces and pressures but contained some fluctuations in front of the building because the flows became quasi-steady (Xu et al., 2021).

Wüthrich et al. (2018) used the total impulse to investigate the momentum exchange with the incoming waves. The total impulse has the advantage of exhibiting less variability than peak forces (Bullock et al., 2007). The total impulse was defined as the surface area under the boundary of the horizontal force time series (Fig. 8c). This boundary is defined by three points a, b, and c (Fig. 8c). In greater detail, point (a) shows the first instant indicating recorded force data above the noise level. Point (b) indicates an instant when the maximum forces occurred, and point (c) displays the data at the end of a quasi-steady phase before falling back to the noise level. Total impulse can be calculated by integrating the positive portion of the horizontal force time series and is expressed by the following equation:

$$I_{tot} = \int_0^{\Delta t} F_H dt \tag{2}$$

Here F_H is the horizontal force in kN, and Δt is the duration between points (a) and (c) in seconds (s). According to Newton's Second Law, we can express total impulse as $F \times \Delta t = m \times \Delta V$, where m is the mass and ΔV is the velocity. That means the estimated total impulse equals the momentum exchange of incoming flows experienced in the vertical buildings. In this study, impact forces, reflection forces, quasi-steady forces, and total impulses were investigated comprehensively later in Fig. 10.

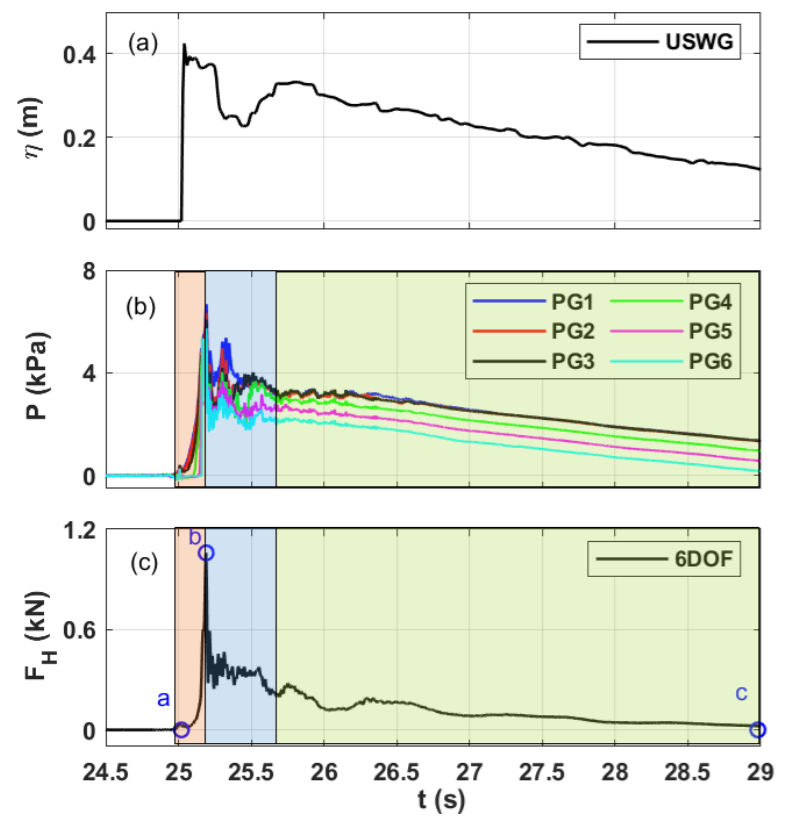


Fig. 8. Temporal variation of (a) free surface displacements measured by USWG1; (b) pressures at six sensors; (c) cross-shore forces measured at 6DOF for baseline configuration of Case 3.

Fig. 9 shows the time series of normalized horizontal forces $F_H/(\rho gBA^2)$, in which F_H (N) is the horizontal force; ρ (kg/m³) is the specific water density; g (m/s²) is the gravitational acceleration, B (m) is the width of building models, and A (m) is the incident wave amplitude. The six-degree-of-freedom-loadcell (6DOF) was utilized to represent the time series of horizontal forces (F_H) in the first building row in Fig. 9. For the most beachfront building row, the rise times take approximately 0.7 s - 1.1 s for cross-shore forces to reach the maximum magnitudes in Case 1 (Fig. 9a) and take 0.04 s - 0.2 s in Cases 2 and 3 overall configurations tested (Fig. 9b, c). The rise time indicates that maximum forces could be observed in the impact phase for Case 2 and Case 3 over four configurations; however, the largest forces could happen during either the reflection or quasi-steady stages of wave impact based on different configurations for Case 1, according to the classification reported in several previous studies (Palermo et al., 2012; Kihara et al., 2015; Xu et al., 2021). In addition, the high-water-level wave cases generated local spikes, and the impulsive-type forces induced by initial impacts in this study are consistent with those in the previous studies (e.g., Bullock et al., 2007; Park et al., 2017).

The effect of structural configurations on wave-induced forces varied for the three wave cases tested. As shown in Fig. 9, the transient-wave impact in Case 1 is broken wave impact, and Cases 2 and 3 are classified as high or low-aeration impacts depending on the configuration, according to Bullock et al. (2007). In Case 1, the transient wave breaks before reaching the building, generating highly aerated turbulent bores. Fig. 9a illustrates the time series of fully-broken waves-induced horizontal forces over

755

756

757758

759

760

761

762

763

764

765

766

767

768

769

770

771

772

773

774

775 776 six configurations, in which the maximum forces measured for configurations with shielding countermeasures are smaller than the forces measured for the baseline configuration for the low-waterlevel case (Case 1). For Cases 2 and 3, low-aeration and high-aeration impacts were recorded, which are characterized by the short rise time and duration of temporally and spatially localized impulsive force. For the high-aeration, such as the SWSB and SB configuration, the transient wave introduced a lot of air into water impinging in the buildings, causing the damped oscillation corresponding to the alternate expansion and compression of air following the time of peak impulsive force (Bullock et al., 2007). For the low-aeration, such as the baseline configuration, the time series of forces illustrate that the water adjacent contained little air entrainment. In contrast to Case 1, countermeasure configurations resulted in larger forces than the baseline in high-water-level cases (Cases 2 and 3) except for the SW configuration in Case 3 (Fig. 9b, c). The SW condition induced the smallest force in Case 3 because the tsunami-like wave impacted the building models as broken waves with smaller velocities than those measured in the SB and SWSB configurations (Fig. 7c). In contrast, the horizontal force measured in the SW configuration in Case 2 showed the largest magnitude among the configurations tested because the seawall served as a ramp, in which water propagated over the seawall to impinge on the building elements directly (Fig. 3e). This phenomenon, called "ramping effects," was also observed in Crespo et al. (2007) and Thomas and Cox (2012). A slight difference in maximum forces for countermeasure configurations was observed in Cases 1 and 2 for all configurations; however, there are significant differences in Case 3 at a higher water level than in Case 1.

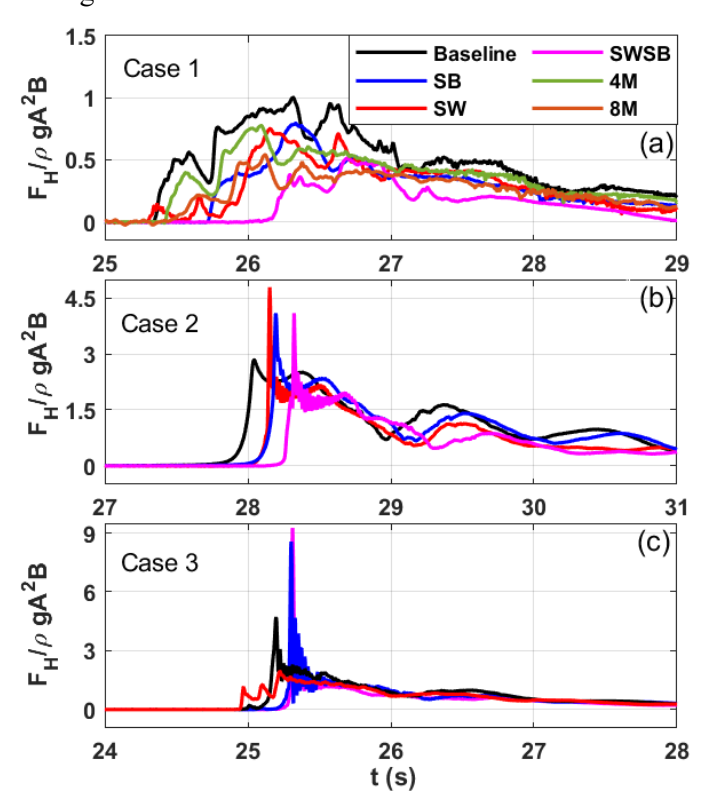


Fig. 9. Time series of normalized forces measured by 6DOF: (a) Case 1; (b) Case 2; (c) Case 3

777

778

779

780

781

782

783

784

785

786

787

788

789

790

791

792

793

794

795

796

797

798

799

800

801

802

803

804

805

806

807

808

809

810

811

812

813

Fig. 10 illustrates the variation of maximum total impulses and maximum horizontal forces in three phases versus relative distance X/L. Particularly, a significant wave and building interaction was witnessed in the first building row; therefore, we installed 6DOF and LC2 in the two building elements to measure horizontal forces induced by the overland flows. The time series of horizontal forces measured in both 6DOF and LC2 have an agreement in the phase over the entire time series; however, there is a discrepancy in the maximum value, which depends on the wave conditions and the interaction phases. LC2 is more sensitive than 6DOF in measuring the sharp peak in the impact stage when the severe interaction occurs, inducing larger deviations in maximum forces compared to the reflection and quasi-steady stages. Especially, the violent interaction between strong waves and building elements (Case 3) contained a lot of random air entrainment in the impact phase, generating a more significant deviation between the two instruments compared to Cases 1 and 2. Therefore, we present the maximum forces and total impulses measured in 6DOF and a deviation bar to represent the difference between the instruments in the most beachfront row. Moreover, from the second to fifth building arrays, maximum forces are located in the quasi-steady phases, ensuring LCs measure the horizontal forces effectively. In general, maximum cross-shore forces in three stages and total impulses decreased with an increase in the relative distance. Horizontal forces significantly decreased when flowing past the first three rows of buildings due to the large wave energy dissipation by breaking waves in this region, while peak forces changed slightly from the third to fifth rows. For the impact stage, maximum forces measured on shielding structures in the first building array for countermeasure configurations are larger than those forces measured for the baseline conditions in high-water-level cases; however, the remaining building rows witnessed smaller forces in countermeasure configurations compared to the baseline. Countermeasure configurations effectively reduced forces in the reflection and quasi-steady phases from the baseline configurations in overall building rows. Regarding total impulses, the SWSB significantly reduced total impulses over the three wave cases. Countermeasure configurations caused a significant reduction in total impulse in the nearest-coast building row; however, there is a slight difference between the total impulse measured for baseline and countermeasure configurations in the remaining arrays over the three wave cases.

Force percent reductions are also expressed using Equation (1) by substituting the maximum elevations with the maximum forces in three phases and total impulses measured in both baseline and countermeasure configurations. Detailed changes in peak forces in the impact phase and total impulse relative to the baseline condition are presented in Tables 4 and 5. These tables show maximum percentages of impulsive force and total impulse difference compared to the baseline in the first row (X/L = 0.15) and the overall percent reduction. The overall value is calculated by averaging the percent reduction of maximum impulsive force or total impulse over five loadcells. The negative percent reduction indicated that the maximum forces and total impulses at countermeasures conditions are larger than those at the baseline. For the impact phase force Case 1, the baseline impulsive force in the first row was reduced to 50% at the SWSB configurations, whereas the 8M configuration resulted in an

impulsive force reduction of 38%. Hence, the combined hard structure is more effective in reducing the impulsive force in the first row. However, there was a significant increase in the impulsive force up to 82% and 90% for SB and SWSB in Case 3, respectively. For the SB and SWSB configurations, the breaking inland flow generated vertically deflected waves, then deflected landward by the momentum of fluid, and finally collapsed in the high elevation of buildings before the continuous flow impacted the entire front face of the first building row. In contrast, for the SW-only configuration without amplification of water elevation offshore due to the submerged breakwater, the seawall significantly dissipated the inland flow propagation, causing wave breaking on the lee side of the seawall. Large wave splashes were generated that hit the buildings initially, which is attributed to some peak impulsive forces shown in Fig. 9c. Regarding the overall percent reduction of impulsive force, the maximum overall percent reduction of impact force over five loadcells reached 68% for the combined hard structures, considering three wave conditions. Although a significant reduction of overall force was recorded in the built environment with the presence of mitigation structures, it is necessary to highlight that the maximum forces are larger than the baseline configuration in the first building row for highwater-level cases. Therefore, it should be taken into consideration for designing structures near coasts."

There are no significant differences among the countermeasure configurations over three wave cases for reflection and quasi-steady forces for all building rows. While all countermeasure configurations caused reductions in total impulse from the baseline configurations, mangroves induced larger total impulses than gray mitigation configurations for Case 1 (Fig. 10). Generally, Tables 4 and 5 also indicate that the SWSB configuration resulted in larger overall percent reductions of impact forces and total impulses compared to individual alternatives.

Table 4. Maximum impulsive force changes

Mitigation	Case 1		Case 2		Case 3	
Strategy	Shoreline at	Overall	Shoreline at	Overall	Shoreline at	Overall
	X/L = 0.15 (%)	(%)	X/L = 0.15 (%)	(%)	X/L = 0.15 (%)	(%)
SB	48	44	-44	7	-82	7
SW	22	45	-68	7	58	48
SWSB	50	68	-44	26	-90	12
4M	25	31	_	_	_	_
8M	38	52	_	_	_	_

Table 5. Maximum total impulse changes

Mitigation	Case 1		Case 2		Case 3	
Strategy	Shoreline at	Overall	Shoreline at	Overall	Shoreline at	Overall
	X/L = 0.15 (%)	(%)	X/L = 0.15 (%)	(%)	X/L = 0.15 (%)	(%)
SB	35	46	10	11	18	16
SW	46	49	23	23	13	27
SWSB	68	73	34	31	29	36
4M	9	-6	_	_	_	_
8M	28	12	_	_	_	_

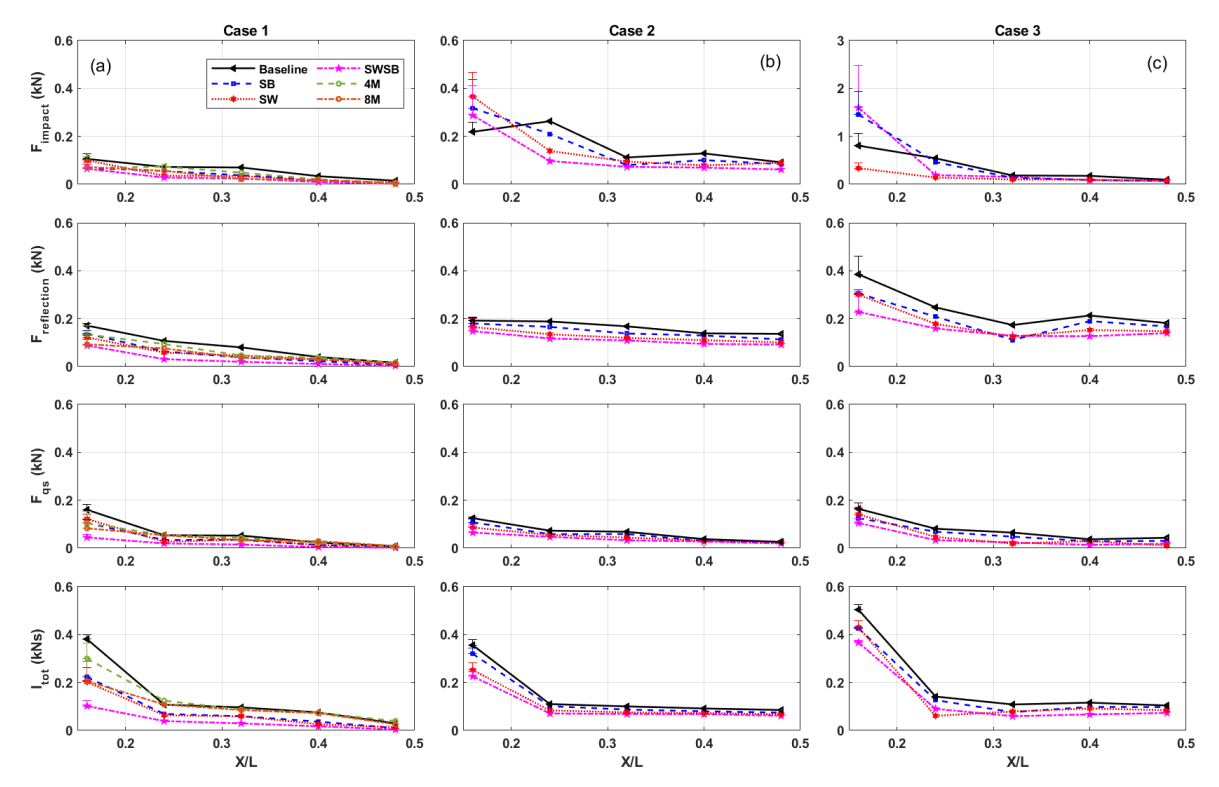


Fig. 10. Variation of maximum horizontal forces in three stages and total impulses.

3.4. Comparison of force reduction factors in Case 1 (low-water-level wave condition)

840841

842 843

844 845

846

847

848

849

850

851

852

853

854

855

856

857

858

859

860

Several previous studies and existing design guidelines in the United States (e.g., FEMA, 2012) and Japanese design standards (e.g., Fukuyama et al., 2011) are primarily used to evaluate wave loading on single buildings without considering the effects of building arrays on overland flows. However, Reese et al. (2007) conducted field observations during the 2006 Java tsunami and showed that while tsunami-caused overland flows damaged buildings along the Pangandaran beach, structures further inland shielded by several commercial buildings near coasts were not seriously damaged. Therefore, analyzing the effects of the presence of nearby buildings on maximum force variation in an urban array is of great importance for engineering design and coastal planning. Moris et al. (2021) comprehensively analyzed the relationship between building row numbers and the change in wave forces and water surface displacements in the condition without any shielding structures through load reduction factor (LRF) and run-up reduction factor (RRF) under the water level of 0.98 m and incident wave amplitudes of 0.13 m and 0.17 m. Following the analysis in Moris et al. (2021), we further evaluate the reduction factor of cross-shore wave-induced forces in countermeasure configurations compared to the baseline cases for the low-water-level condition (A = 0.21 m and h = 0.98m). The load reduction factor can be expressed through a fraction of $\left(F_c^{(i)}\right)_{\max}/\left(F_b^{(1)}\right)_{\max}$, in which $\left(F_b^{(1)}\right)_{\max}$ is the maximum force measured by 6DOF located in the first building element in the baseline case, $\left(F_c^{(i)}\right)_{\max}$ is the maximum force at

each of the five loadcells (6DOF to LC6) in the countermeasure configurations. The presence of building rows is represented through the relative distance to each loadcell *X/L*.

Fig. 11 illustrates the load reduction factor as a function of the relative distance, which is covered by a 1-term exponential upper boundary curve (black solid line):

865
$$\frac{(F_c^{(i)})_{\text{max}}}{(F_b^{(i)})_{\text{max}}} = 2.65e^{-6.1X/L}$$
 (3)

The empirical boundary curve, containing output as a fractional term and non-dimensional input, allows its application to a wide range of macro-roughness sizes and shapes (Thomas and Cox, 2012). Generally, there was a monotonic decrease in load reduction factors with increased relative distance X/L. The highest load reduction factor was 1 in the baseline configuration in the first building row (no reduction). The overland tsunami-like wave broke near the end of the slope (x = 31.7 m and z = 1.0 m), inducing turbulent bores that propagated and impacted the most seaward building row (X/L = 0.15), whereas the first building row dissipated the most extensive turbulent energies of incoming flows before reaching the remaining rows. Therefore, the greatest reduction was observed from X/L = 0.15 to X/L = 0.24, in which the load reduction value decreased by 0.40 (40%) for the baseline condition. The reduction factors witnessed a significant decline of approximately 0.8 (80%) at the fourth building row (X/L = 0.4), compared to that measured at the first building row, meaning maximum horizontal forces decreased four times with three rows sheltering the structure from wave interaction. Slight decreases to below 0.20 were seen in the force fraction for all configurations in the fifth building row.

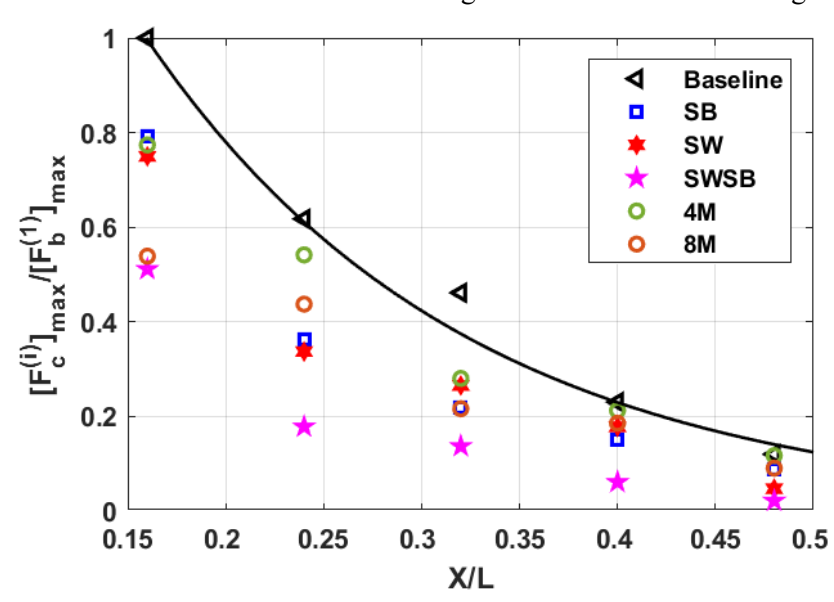


Fig. 11. Comparison of green and gray structures in load reduction factors versus relative distances for Case 1 (low-water-level condition).

Fig. 11 also compares force reduction factors due to the green and gray mitigation measures. At the first row, the maximum baseline force is reduced by approximately 23% for the SB and SW configurations separately and the four rows of mangroves (4M). Therefore, the presence of individual

hard structures and 4M indicated a similar capacity in alleviating maximum force in the most seaward building. Moreover, approximately 50% of the combined SBSW configuration was witnessed in the first row, slightly higher by 4% for the eight rows of mangroves. It is interesting to note that the two separate treatments and 4-row mangrove configurations show a relatively linear combination for the SWSB and 8M configuration at the first row since the linear combination does not hold at the other locations. In the second row, for example, the SB and SW configurations each show a reduction of approximately 50% relative to the baseline condition. However, the SWSB configuration shows a reduction of approximately 70%. In any case, the SWSB configuration shows a significant reduction in wave force relative to the baseline condition for this case. Therefore, the presence of both the seawall and submerged breakwater dramatically contributed to reducing the loads generated by tsunami-like wave-caused overflows in the low-water-level condition, suggesting that combined mitigation countermeasures may outperform individual solutions. It should be noted, however, that the SWSB configuration did not improve the impact force for Cases 2 and 3.

For the use of mangroves, the 8M configuration reduced the maximum baseline force, doubling the performance of the 4M. This indicates that a moderate increase in cross-shore forest width could have a significant impact on reducing wave forces for certain incident wave conditions. However, some caution is warranted because scale effects will exaggerate the dissipative benefits. Moreover, there was no consideration of the survivability of the mangroves (uprooting, breakage) during inundation. In any case, the positive results here would suggest that further research for prototype conditions should be considered in combination with conventional coastal structures.

3.5. Comparison of force reduction factors in Case 2 and Case 3 (high-water-level wave conditions)

Fig. 12 shows the load reduction factors plotted against relative distance for the gray structure configurations only in the high-water-level wave conditions. Similar to the low-water-level wave case, a monotonic decreasing trend for maximum forces was observed for several loadcell locations. The force reduction factor values in the first row for the countermeasure configurations are larger than those for the baseline configuration due to the amplification of the impact forces. In particular, the SWSB condition induced an extensive increase up to twice the baseline in the first row. However, the force reduction factor dramatically decreased by 2.5 and 8 times for the SWSB condition during the first two arrays in Cases 2 and 3, respectively, with the load reduction factor values remaining relatively stable at around 0.6 (Case 2) and 0.2 (Case 3) for the four remaining building rows (X/L > 0.24).

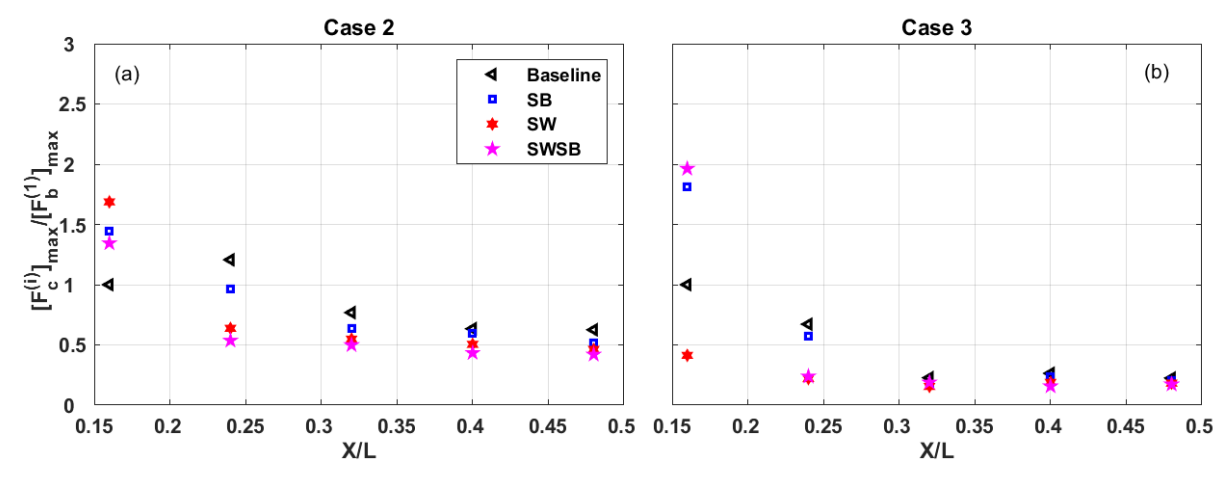


Fig. 12. Force reduction factor versus the relative cross-shore distance *X/L* in Cases 2 &3 (high-water-level cases).

4. Discussion

919 920

921

922 923

924 925

926

927

928

929

930

931

932

933

934

935

936

937

938

939

940

941

942

943

944

945

946

947

948

A scaled physical experiment investigated the performance of gray and green countermeasures against tsunami-like wave impacts on the urban environment. This study provides a comprehensive experimental analysis of the transformation of tsunami-like forces, pressures, and hydrodynamics in the inland area in the presence of different countermeasure configurations subject to three varying incident initial wave conditions. The results show that tsunami-like wave forces highly depend on wave-breaking characteristics affected by the dimensions, positions, and geometries of countermeasures, as well as initial wave conditions.

Several experimental considerations and idealizations must be acknowledged in the interpretation of the results. Firstly, the countermeasure configurations tested here represent an idealization of submerged breakwaters, seawalls, and mangrove trunk-prop root systems. The dimensions and locations of mitigation alternatives were fixed for the whole test trial in the current experiment. However, previous studies (e.g., Thomas and Cox, 2012) highlighted that the heights and positions of seawalls affected force reduction factors. In addition, several studies investigating wave and currents around submerged breakwaters (e.g., Johnson et al., 2005) or shoreline response on the lee side of submerged breakwaters (e.g., Ranasinghe and Turner, 2006) generally accepted that the proximity of submerged breakwater to the shoreline affects the wave transformation. Therefore, additional structural parameters and locations could be modified to verify the effectiveness of structural countermeasures in tsunami overflow reduction thoroughly. Similarly, mangrove forests in nature will comprise multiple species with spatially varying tree ages, stem densities, and growth stages; the projected area associated with these heterogeneous natural systems will be affected by the water depth, ultimately affecting wave attenuation and resulting loads on inland structures (e.g., Kelty et al., 2022). Future studies may consider additional forest densities or configurations to represent these natural systems. Secondly, three incident wave trials varied the wave amplitudes and water levels considered in this study. However, the current study only investigated the relationship between force reduction factors and the relative distance from

949

950

951

952

953

954

955

956957

958

959

960

961

962

963

964

965

966

967

968

969

970

971

972

973

974

975

976

977

978

979

980

981

982

983

984

985

each building row to the shoreline. Therefore, the analysis of force reduction factors must be further developed by including relationships between the relative distance, water depth, and incident wave parameters. Further, a comparison of structural and natural countermeasures was only performed for the low-water-level wave case (Case 1), for which conditions tested by Tomiczek et al. (2020a) overlapped conditions tested in the structural countermeasure experiments. Future work must consider the comparative performance of gray and green countermeasures under other wave conditions. For example, a comparison of force reduction factors between gray structures and mangroves for the highwater-level cases will be analyzed through numerical modeling and extended for other incident wave conditions.

Besides long-wave disaster prevention, additional work is required to evaluate the performance of the mitigation structures during normal and storm conditions. Wave conditions containing regular, irregular, and storm waves with and without background currents must be tested to fully acknowledge these structures' mechanisms. Tomiczek et al. (2020a) observed that the presence of currents was associated with an increase in water levels and increased impulsive forces exerted on vertical buildings, potentially causing the contribution to failures of structures under long-lasting or extreme conditions.

It is important to note that the experiments conducted here were performed at a reduced geometric scale (1:16). While the geometric scale was selected as large as possible given the dimensions and capabilities of the DWB, scaling effects may play a significant role in measured forces under countermeasure configurations, particularly for mangrove configurations where friction may be enhanced in reduced scale models. The period of transient wave in the 1:16 scale at Case 1 is about 15 s; thus, the prototype period is 60 s, considering the Froude scaling. This is much shorter than an actual tsunami wave (5 to 20 min) but quite larger than general storm waves (< 20 s), so the term "tsunamilike wave" is used to represent the wave condition. Additional dimensionless numbers based on other similarity laws were designed, with values exceeding the critical values proposed by Peakall and Warbuton (1996). Particularly, the minimum Weber number (fraction between the inertia and surface tension force) is 1400 during the quasi-steady stages compared to its critical value of 100. The minimum Reynolds number of 20000 for the size of mangrove roots (0.0025 m), enabling the generation of the turbulent wake, while the critical value of Reynolds number is only 2000 as suggested in Peakall and Warbuton (1996). Nonetheless, the effect of atmospheric pressure in Euler similarity is neglected because of the free surface nature of the phenomenon. The Cauchy similarity induced the structures to behave too stiffly compared to the real structures, resulting in the elasticity of structure models cannot be scaled. However, the severe impact of the tsunami-like waves on building elements contains a lot of air entrainment, which influences the maximum forces exerted on the building elements, requiring the consideration of the Cauchy similarity. Further investigation of the laboratory experiment in different scales is needed to investigate the potential scale effects on the wave transformation, including wave breaking and impacts on structures, and the comparison of the protective performance of each mitigation alternative. Therefore, results derived from this study must be interpreted with caution, and future

prototype-scale physical modeling, numerical modeling, and field observations are required to verify the performance of gray and green countermeasure systems in tsunami hazard mitigation.

In general, the results of these experiments can have significant implications for coastal planning for tsunami or coastal flood hazard mitigation. Results indicate that, in general, multi-tiered solutions (i.e., SWSB) outperform individual countermeasures in reducing water surface elevations, velocities, and loads in the built environment for overland flow conditions. Further, while additional work is needed to verify performance under a range of incident hydrodynamic conditions, these results suggest a measurable contribution of natural infrastructure (mangroves) to mitigate overland flow velocities and loads on inland structures, providing sufficient cross-shore widths. Future work may further investigate the combined performance of green and gray systems (e.g., submerged breakwater + mangroves or seawall + mangroves) in reducing coastal flood hazards during varied overland flow conditions.

5. Conclusions

The physical model experiment investigated the effects of countermeasure configurations, including a seawall, a submerged breakwater, a combined seawall and submerged breakwater, and mangrove forests of two moderate cross-shore widths against a tsunami-like wave-induced overland flow on the built environment. This study analyzed wave forces and inland hydrodynamic characteristics on a series of building rows. Based on the results of these experiments, the following conclusions are presented:

- 1. The presence of countermeasures influenced flow depths recorded in the inland area. While all mitigating structures reduced flow depths in front of the seaward-most building array for the low-water-level case, the SB configuration amplified the flow depth by a maximum of 33% in the high-water-depth cases. Averaged percent reductions of flow depth over the landward area reached 26%, 30%, and 53% in the SB, SW, and SWSB conditions over three wave cases, whereas, for Case 1, the average water surface elevation was amplified at 38% and 35% in 4M and 8M configurations, respectively.
- 2. Bed conditions highly affected the leading edge of cross-shore velocities. Tsunami-like wave propagation in the dry bed was faster than in the wet bed. The presence of countermeasure configurations induced smaller cross-shore velocities compared to the baseline configuration. There is no significant difference in peak velocities at the first building row recorded for the green and gray structure configurations for the low-water-level case. Averaged percentages of velocity reductions were up to 21%, 23%, 34%, 20%, and 30% over three transient wave (tsunami-like wave) cases at the SB, SW, SWSB, 4M, and 8M configurations, respectively. Generally, the SW configuration performed better than the SB configuration in alleviating

- horizontal velocities around the buildings, while the SWSB was more effective than other configurations.
 - 3. Countermeasure configurations significantly reduced maximum forces in the low-water level case. However, the presence of a submerged breakwater in the configurations amplified the impact force in the first building row compared to the baseline condition for the high-water-level cases. For the low-water-level case, the SWSB reduced the peak impulsive force by 50% relative to the baseline configuration, while for high-water-level conditions, the SWSB configuration resulted in an increase of impulsive force of up to 90% in the first building array. However, the SWSB induced the smallest magnitudes of reflection, quasi-steady forces, and total impulses compared to other configurations.
 - 4. In the low-water-level case, a 1-term exponential upper boundary curve was applied to examine the force reduction factor as a function of the relative distance between the building elements and shorelines. Load reduction factors decreased four times in the fourth building row that was shielded by the three seaward rows of buildings.
 - 5. Compared to the near-coast areas protected by green structure configurations under the low-water-level wave case, both the individual SB and SW generated a similar load reduction factor to the 4M, equal to relatively twice the 8M and SWSB condition in the first row. The presence of both seawall and submerged breakwater (SWSB) was more effective than individual configurations in reducing wave loadings on all building rows in the low-water-level case.

This study conducted a unique scaled physical model experiment to evaluate the performance of shielding structures against overland flow effects; however, the physical modeling results cannot generalize the performance of countermeasures as we only utilized three wave conditions over the fixed geometry and bathymetry conditions. Additional work is needed to clarify the potential and limitations of leveraging combined countermeasures for coastal protection. Future physical and numerical tests are required to investigate the varying dimensions and positions of green and gray structures on force reduction. The effect of countermeasures under regular and random wave cases with/without currents is also worthy of further investigation.

Credit authorship contribution statement

Hai Van Dang: Methodology, Investigation, Conceptualization, Data curation, Formal analysis, Visualization, Writing-original draft, Writing-Review & Editing. Hyoungsu Park: Methodology, Investigation, Conceptualization, Writing-Review & Editing, Supervision. Sungwon Shin: Methodology, Investigation, Conceptualization, Data curation, Writing-Review & Editing, Supervision, Fund acquisition. Tori Tomiczek: Conceptualization, Writing-Review & Editing, Supervision, Fund acquisition. Daniel T. Cox: Conceptualization, Writing-Review & Editing, Supervision, Fund acquisition. Eunju Lee: Methodology, Investigation, Writing-Review & Editing. Dayeon Lee: Data

1058 curation, Writing-Review & Editing. **Pedro Lomonaco**: Conceptualization, Experiment Design, 1059 Writing-Review & Editing.

Acknowledgment

Personnel on this project were funded by the National Science Foundation through multiple awards: Cox NSF-1661315 and NSF-2110439, Kennedy NSF-1661015, Tomiczek NSF-1825080 and NSF-2110262. This material in this study is also partially supported by National Research Foundation in Korea under awards 2022R1F1A1071641. The O.H. Hinsdale Wave Research Laboratory is partially supported through the Natural Hazards Engineering Research Infrastructure program of National Science Foundation through award NSF-2037914. The experimental data are available on DesignSafe.org at https://doi.org/10.17603/ds2-j0j1-5827. The authors thank Andrew Kennedy and Patrick Lynett for their contributions to the overall experimental design and Joaquin Pablo Moris, and Adam Keen for conducting experimental testing.

Appendix

A1. Photos of instrumentation setup in the experiment

 Fig. A1 shows the experimental instrument, including wave gauges, ultrasonic wave gauges, acoustic Doppler velocimeters, loadcells, a six-degree-of-freedom loadcell, and pressure sensors.

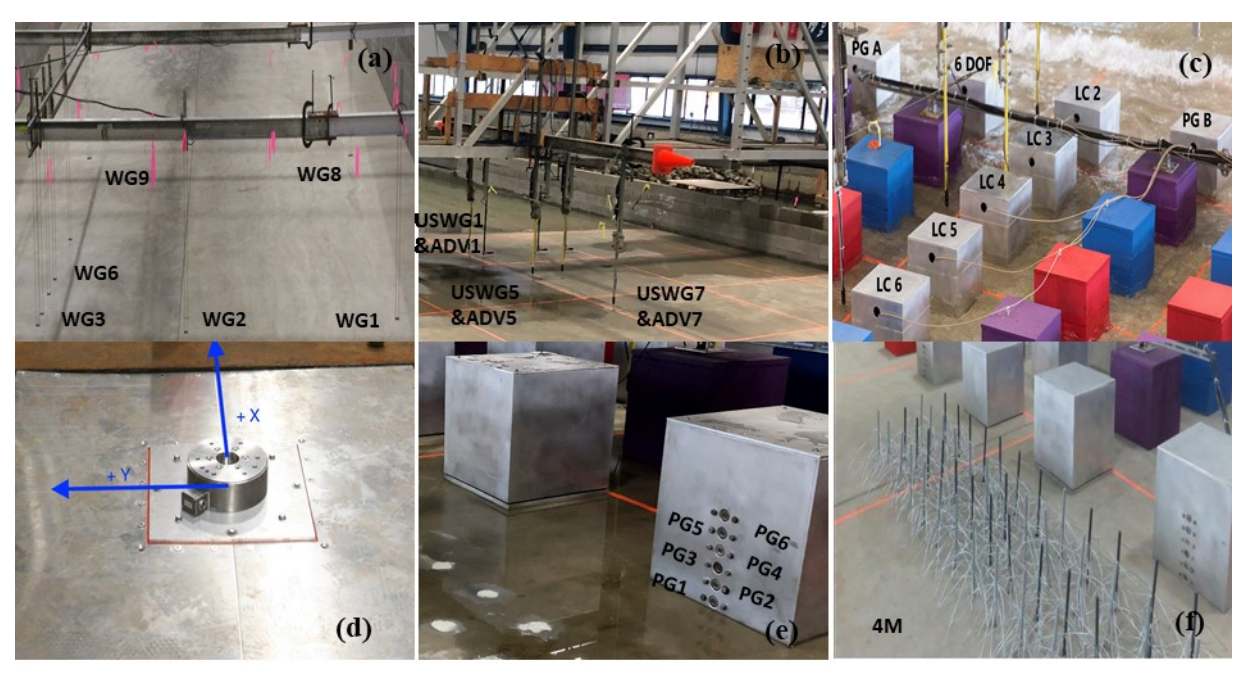
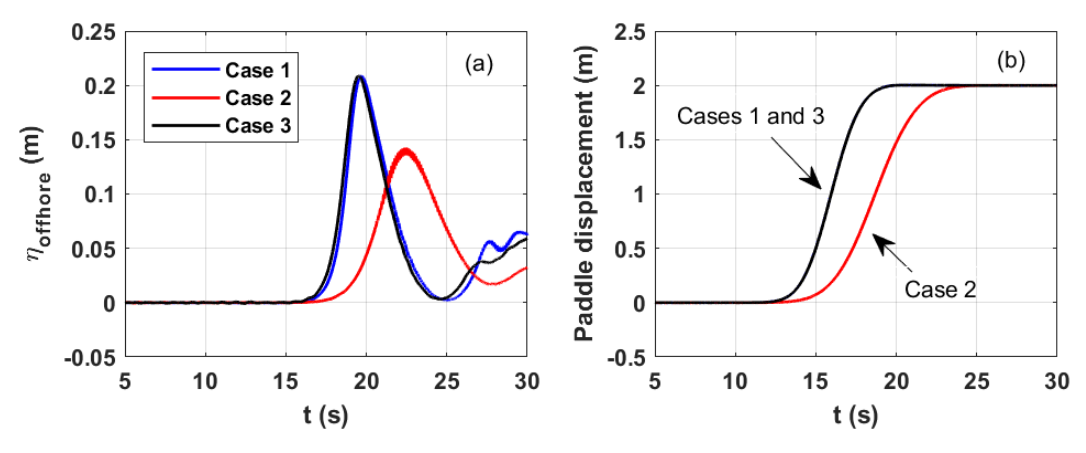


Fig. A.1. Instrumentation layouts and details: (a) Wire resistance wave gauges; (b) collocated ultrasonic wave gauges (USWGs) with acoustic Doppler velocimeters (ADVs); (c) Instrumented buildings (identified by 8 silver boxes); (d) Six-degree-of-freedom loadcell; (e) pressure gauges; (f) mangrove forest.

A2. Wave conditions

108710881089

Fig. A2a presents the time series of water surface elevations in three tsunami-like wave cases for the baseline conditions. The time series of paddle displacements are shown in Fig. A2b. Cases 1 and 3 indicate the same rise time (overlapped in Fig. A2b), which is shorter than the rise time for Case 2.



1090 1091

1092

Fig. A.2. (a) Time series of offshore water surface elevations measured at WG2 and (b) paddle displacements measured by wmdisp for three wave trials in the baseline condition.

1093 1094

A3. Data processing techniques

1095 1096

1097

1098

1099

1100

1101

1102

1103

1104

1105

1106

1107

1108

1109

1110

1111

1112

1113

1114

1115

1116

Fig. A3 shows an example of data processed from one trial for Case 2 with a water depth of 1.1 m and wave amplitude of 0.14 m for a baseline test (i.e., no green and gray mitigation alternatives). Fig. Fig. A3a illustrates the piston displacements and free surface profiles on the wavemaker. In addition, Fig. A3b shows offshore water elevations measured by WG3, WG6, and WG9 located along the sloped section. The first peak of the incident waves slightly changed in the mild slope. The water elevation near the wavemaker represents a symmetric positive incident surge; however, the waveform becomes asymmetric in WG3, WG6, and WG9 at the start of the sloping beach. Each Fig. A3c and Fig. A3d shows onshore flow depths from USWGs and cross-shore (wave direction) velocities from ADVs in the inland area. The leading edges of wave velocities were not easy to capture from ADVs for the lowwater-level case of 0.98 m (Case 1), but they are measured clearly in the wave trials with a high-waterlevel case of 1.1 m (Case 2 and Case 3). Fig. A3e illustrates the example of the time histories of force data measured at in-line loadcells LC2, LC4, and LC6. In the initial impact on the most seaward building row (measured by LC2), the maximum force occurred in the initial impulse, followed by run-up and quasi-steady phases with their maximum magnitudes of approximately 50% – 80% of the impulsive peak (Fig. A3e). The initial spike was visually observed in the force data and was also seen in the hydrodynamic pressure data in the building model nearest to the shoreline (Fig. A3f). The 6DOF was also installed to measure forces and moments in three directions in the seaward-most building row. However, the cross-shore horizontal (x-directed) wave-induced forces are much larger than those in the y and z directions. Therefore, this study solely focuses on streamwise forces in the force reduction analysis. All other cases were processed in a similar method to ensure that the instrumental equipment was working correctly.

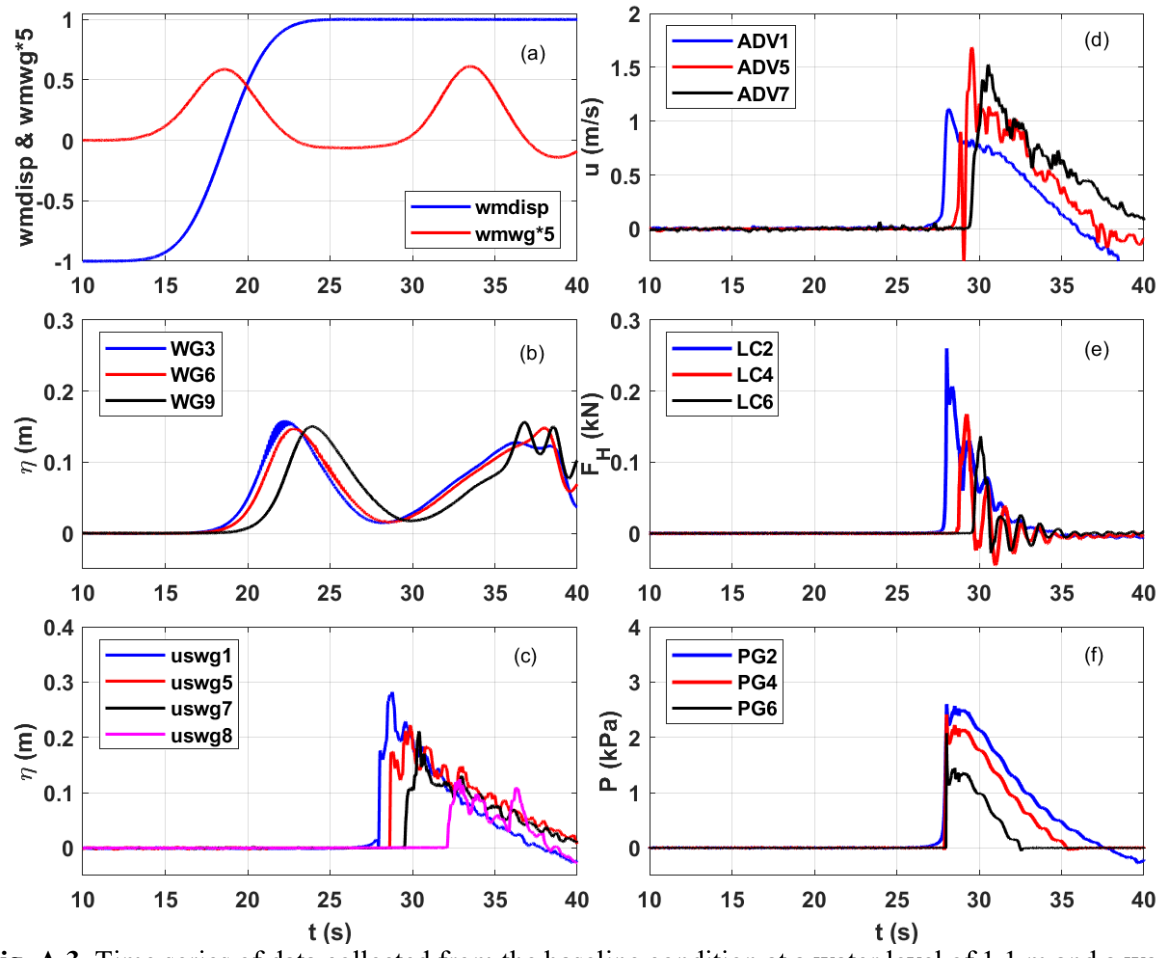


Fig. A.3. Time series of data collected from the baseline condition at a water level of 1.1 m and a wave amplitude of 0.14 m: (a) paddle movement and wavemaker wave gauge, (b) offshore wire resistance wave gauges, (c) ultrasonic wave gauges, (d) Cross-shore velocity component measured by acoustic Doppler velocimeters, (e) in-line horizontal loadcells, (f) pressure sensors.

References

 $\begin{array}{c} 1117 \\ 1118 \end{array}$

Aghababaei, M., Koliou, M., Paal, S. G., 2018. Performance assessment of building infrastructure impacted by the 2017 Hurricane Harvey in the Port Aransas region. Journal of Performance of Constructed Facilities, 32(5), 4018069. doi:10.1061/(ASCE)CF.1943-5509.0001215

Anderson, M. E., Smith, J. M., 2014. Wave attenuation by flexible, idealized salt marsh vegetation. Coastal Engineering, 83, 82–92. doi: 10.1016/j.coastaleng.2013.10.004

Baldock, T., Cox, D., Maddux, T., Killian, J., Fayler, L., 2009. Kinematics of breaking tsunami wavefronts: A data set from large scale laboratory experiments. Coastal Engineering, 56 (5–6), 506–516. https://doi.org/10.1016/j.coastaleng.2008.10.011

Bridges, T. S., King, J. K., Simm, J. D., Beck, M. W., Collins, G., Lodder, Q., Mohan, R. K., 2021. International Guidelines on Natural and Nature-Based Features for Flood Risk Management. Vicksburg, MS: U.S. Army Engineer Research and Development Center. http://dx.doi.org/10.21079/11681/41946

Browder, G., Ozment, S., Rehberger Bescos, I., Gartner, T., Lange, G. M., 2019. Integrating Green and Gray: Creating Next Generation Infrastructure. Washington, DC: World Bank Group. 9781569739556.pdf

Bullock, G., Obhrai, C., Peregrine, D., Bredmose, H., 2007. Violent breaking wave impacts. Part 1: Results from large-scale regular wave tests on vertical and sloping walls. Coastal Engineering, 54 (8), 602–617. https://doi.org/10.1016/j.coastaleng.2006.12.002

- 1144 Chang, C.-W., Mori, N., 2021. Green infrastructure for the reduction of coastal disasters: a review of 1145 the protective role of coastal forests against tsunami, storm surge, and wind waves. Coastal 1146 Engineering Journal 63(3), 370-385. https://doi.org/10.1080/21664250.2021.1929742
- 1147 Chang, C.-W., Mori, N., Tsuruta, N., Suzuki, K., 2019. Estimation of wave force coefficients on Mangrove models. JSCE Proc. B2 75, 1105–1110. https://doi.org/10.2208/kaigan.75.I_1105
- Church, J.A., Clark, P.U., Cazenave, A., Gregory, J.M., Jevrejeva, S., Levermann, A., Merrifield, M.A., Milne, G.A., Nerem, R.S., Nunn, P.D., Payne, A.J., Pfeffer, W.T., Stammer, D., Unnikrishnan, A.S.,
- 1151 2013. Sea level change. In: Stocker, T.F., Qin, D., Plattner, G.-K., Tignor, M., Allen, S.K.,
- Boschung, J., Nauels, A., Xia, Y., Bex, V., Midgley, P.M. (Eds.), Climate Change 2013: The Physical Science Basis. Contribution of Working Group I to the Fifth Assessment Report of the
- Intergovernmental Panel on Climate Change. Cambridge University Press, Cambridge, United Kingdom and New York, NY, USA. doi: 10.1017/CBO9781107415324.026
- 1156 Cokgor, S., Kapdasli, M. S., 2005. Performance of submerged breakwaters as environmental friendly 1157 coastal structures. In Environmentally friendly coastal protection, Springer: 211–218. DOI:10.1007/1-4020-3301-X 13
- Cox, D., Arikawa, T., Barbosa, A., Guannel, G., Inazu, D., Kennedy, A., Li, Y., Mori. N., Perry, Kwasi.,
 Prevatt, D., Roueche, D., Shimozono, T., Simpson, C., Shimakawa, E., Shimura, T., 2019.
 Hurricanes Irma and Maria post-event survey in US Virgin Islands. Coastal Engineering Journal,
 61 (2), 121–134. https://doi.org/10.1080/21664250.2018.1558920
- Crespo, A., Gómez–Gesteira, M., Dalrymple, R., 2007. 3D SPH simulation of large waves mitigation with a dike. Journal of Hydraulic Research, 45 (5), 631–642. https://doi.org/10.1080/00221686.2007.9521799
- 1166 Cross, R., 1967. Tsunami surge forces. Journal of Waterway and Harbors Divisions, 93(4), 201–231. https://doi.org/10.1061/JWHEAU.0000528
- Dahdouh-Guebas, F., Koedam, N., 2006. Coastal vegetation and the Asian tsunami. Science. 311:37–38. DOI: 10.1126/science.311.5757.37
- Dalrymple, R. A., Kirby, J. T., Hwang, P. A., 1984. Wave diffraction due to areas of energy dissipation.

 Journal of Waterway, Port, Coastal, and Ocean Engineering. 110, 67–79. doi: 10.1061/(ASCE)0733-950X1984110:1(67)
- Dalrymple, R.A., Kriebel, D.L., 2005. Lessons in Engineering from the Tsunami in Thailand. The Bridge, U.S. National Academy of Engineering, 35, 2.
- Danielsen, F., Sorensen, M, K., Olwig, M. F., Selvam, V., Parish, F., Burgess, N. D., Hiraishi, T., Karunagaran, V. M., Rasmussen, M. S., Hansen, L. B., Quartom, A., Suryadiputra, N., 2005. The Asian tsunami: a protective role for coastal vegetation. Science. 310:643–643. <u>DOI:</u> 10.1126/science.1118387
- Das, S., Vincent, J. R., 2009. Mangroves Protected Villages and Reduced Death Toll during Indian Super Cyclone. Proceedings of the National Academy of Sciences 106 (18): 7357–7360. doi:10.1073/pnas.0810440106
- Dong, S., Abolfathi, S., Salauddin, M., Tan, Z.H., Pearson, J.M., 2020. Enhancing climate resilience of vertical seawall with retrofitting a physical modelling study. Applied Ocean Research. 103, 102331 https://doi.org/10.1016/j.apor.2020.102331
- Duncan, S., Cox, D., Barbosa, A. R., Lomónaco, P., Park, H., Alam, M. S., Yu, C., 2021. Physical modeling of progressive damage and failure of wood–frame coastal residential structures due to surge and wave forces. Coastal Engineering, 103959. https://doi.org/10.1016/j.coastaleng.2021.103959
- Eamon, C.D., Fitzpatrick, P., Truax, D.D., 2007. Observations of structural damage caused by hurricane Katrina on the Mississippi Gulf coast. Journal of Performance of Constructed Facilities. 21 (2), 1191 https://doi.org/10.1061/(asce)0887-3828
- Esteban, M., Tsimopoulou, V., Mikami, T., Yun, N., Suppasri, A., Shibayama, T., 2013. Recent tsunamis events and preparedness: Development of tsunami awareness in Indonesia, Chile and Japan. International Journal of Disaster Risk Reduction, 5, 84–97. https://doi.org/10.1016/j.ijdrr.2013.07.002
- EurOtop, 2018. Wave Overtopping of Sea Defences and Related Structures: Assessment Manual. <u>The</u>
 Effects of Seawalls on the Beach: Part I, An Updated Literature Review (jstor.org)
- 1198 FEMA, 2012. Fema P-646, Guidelines for Design of Structures for Vertical Evacuation from Tsunamis.

- Fukuyama, H., Kato, H., Ishihara, T., Tajiri, S., Tani, M., Okuda, Y., Nakano, Y., 2011. Structural Design Requirement on the Tsunami Evacuation Buildings. UJNR, Tokyo. UJNR 2013 Tsunami Manuscript.pdf (nehrp.gov)
- Gedan, KB., Kirwan, M. L., Wolanski, E., Barbier, E. B., Silliman, B R., 2011. The present and future role of coastal wetland vegetation in protecting shorelines: answering recent challenges to the paradigm. Climate Change. 106:7–29. <u>DOI 10.1007/s10584-010-0003-7</u>
- Goda, K., Mori, N., Yasuda, T., Prasetyo, A., Muhammad, A., Tsujio, D., 2019. "Cascading Geological
 Hazards and Risks of the 2018 Sulawesi Indonesia Earthquake and Sensitivity Analysis of Tsunami
 Inundation Simulations. Frontiers in Earth Sci 7:261. doi: 10.3389/feart.2019.00261
- Goring, D. G., 1978. Tsunamis the propagation of long waves onto a shelf. Laboratory of Hydraulics and water resources. California Institute of Technology. DOI: 10.7907/Z9W957BN
- Granek, E. F., Ruttenberg, B. I., 2007. Protective Capacity of Mangroves during Tropical Storms: A
 Case Study from 'Wilma' and 'Gamma' in Belize. Marine Ecology Progress Series 343: 101–105.
 doi:10.3354/meps07141
- Ha, T., Yoo, J., Han, S., Cho, Y.–S., 2014. Numerical study on tsunami hazard mitigation using a submerged breakwater. The Scientific World Journal. https://doi.org/10.1155/2014/863202
- Heller, V., 2019. Tsunami Science and Engineering II. Multidisciplinary Digital Publishing Institute.

 Journal of Marine science and Engineering, 7(9), 319. https://doi.org/10.3390/jmse7090319
- 1217 Irtem, E., Seyfioglu, E., Kabdasli, M. S., 2012. Comparison of the effects of permeable, impermeable
 1218 and monolithic vertical—face submerged breakwaters on tsunami run-up height. The Twenty—
 1219 second International Offshore and Polar Engineering Conference, International Society of Offshore
 1220 and Polar Engineers: 2012.
- 1221 http://publications.isope.org/proceedings/ISOPE/ISOPE%202012/data/papers/vol3/2012-TPC-931Irtem.pdf
- 1223 Irtem, E., Seyfioglu, E., Kabdasli, S., 2011. Experimental investigation on the effects of submerged 1224 breakwaters on tsunami run-up height. Journal of Coastal Research, 516–520. 1225 https://www.jstor.org/stable/26482226
- Jeffreys, H., 1944. Note on the offshore bar problem and reflection from a bar. Grt. Brrit. Ministry of Supply, Wave Report, 3.
- Jeng, D.–S., Schacht, C., Lemckert, C., 2005. Experimental study on ocean waves propagating over a submerged breakwater in front of a vertical seawall. Ocean Engineering, 32 (17–18), 2231–2240. https://doi.org/10.1016/j.oceaneng.2004.12.015
- Johnson, H. K., Karambas, T. V., Avgeris, I., Zanuttigh, B., Gonzalez-Marco, D., Caceres, I., 2005.
 Modelling of waves and currents around submerged breakwaters. Coastal Engineering, 52(10-11),
 949-969. https://doi.org/10.1016/j.coastaleng.2005.09.011
- Kathiresan, K., Rajendran, N., 2005. Coastal mangrove forests mitigated tsunami. Estuarine Coastal Shelf Science. 65, 601–606. https://doi.org/10.1016/j.ecss.2005.06.022
- Kelty, K., Tomiczek, T., Cox, D.T., Lomonaco. P., Mitchell. W., 2022. Prototype-Scale Physical Model
 of Wave Attenuation Through a Mangrove Forest of Moderate Cross-Shore Thickness: LiDAR Based Characterization and Reynolds Scaling for Engineering With Nature. Frontiers in Marine
 Science, 8:780946. doi: 10.3389/fmars.2021.780946
- Kihara, N., Arikawa, T., Asai, T., Hasebe, M., Ikeya, T., Inoue, S., Kaida, H., Matsutomi, H., Nakano,
 Y., Okuda, Y., 2021. A physical model of tsunami inundation and wave pressures for an idealized
 coastal industrial site. Coastal Engineering, 103970.
 https://doi.org/10.1016/j.coastaleng.2021.103970
- Kihara, N., Niida, Y., Takabatake, D., Kaida, H., Shibayama, A., Miyagawa, Y., 2015. Large-scale experiments on tsunami-induced pressure on a vertical tide wall. Coastal Engineering, 99, 46 63. https://doi.org/10.1016/j.coastaleng.2015.02.009
- Kobayashi, N., Wurjanto, A., 1989. Wave transmission over submerged breakwaters. Journal of waterway, port, coastal, and ocean engineering, 115 (5), 662–680. https://doi.org/10.1061/(ASCE)0733-950X(1989)115:5(662)
- Koraim, A., Heikal, E., Zaid, A. A., 2014. Hydrodynamic characteristics of porous seawall protected by submerged breakwater. Applied ocean research, 46, 1–14. https://doi.org/10.1016/j.apor.2014.01.003

- 1253 Koshimura, S., Oie, T., Yanagisawa, H., Imamura, F., 2009. Developing fragility functions for tsunami 1254 damage estimation using numerical model and post–tsunami data from Banda Aceh, Indonesia. 1255 Coastal Engineering Journal, 51 (3), 243–273. https://doi.org/10.1142/S0578563409002004
- 1256 Krauss, K. W., Doyle, T. W., Doyle, T. J., Swarzenski, C. M., From, A. S., Day, R. H., Conner, W. H.,
 1257 2009. Water Level Observations in Mangrove Swamps during Two Hurricanes in Florida. Wetlands,
 1258 29 (1): 142–149. doi:10.1672/07-232.1
- Lee, D., Park, H., Ha, T., Shin, S., Cox, D., 2022. Numerical Modeling of hydrodynamics on an elevated
 resident structure from varied wave and surge conditions using OpenFOAM. Coastal Engineering,
 178, 104204. https://doi.org/10.1016/j.coastaleng.2022.104204
- Li, X., Zhang, W., 2019. 3D numerical simulation of wave transmission for low–crested and submerged breakwaters. Coastal Engineering, 152, 103517. https://doi.org/10.1016/j.coastaleng.2019.103517
- Lomonaco, P., Barbosa, A., Cox, D., Johnson, T., Keen, A., Kennedy, A., Lynett, P., Barra, J. M., Park, H., Shin, S., 2020. Loading and structural response of developed shorelines under waves, surge, and tsunami overland flow hazards. Coastal Engineering Proceedings, (36v), 36–36. https://doi.org/10.9753/icce.v36v.structures.36
- Lukkunaprasit, P., Ruangrassamee, A., 2008. Building damage in Thailand in the 2004 Indian Ocean tsunami and clues for tsunami–resistant design. The IES Journal Part A: Civil & Structural Engineering, 1 (1), 17–30. https://doi.org/10.1080/19373260701620162
- Madsen, P. A., Fuhrman, D. R., Schaffer, H. A., 2008. On the solitary wave paradigm for tsunamis. Journal of Geophysical Research, 113, C12012. doi:10.1029/2008JC004932
- 1273 Marois, D.E., Mitsch, W.J., 2015. Coastal protection from tsunamis and cyclones provided by mangrove 1274 wetlands—a review. International Journal of Biodiversity Science, Ecosystem Services & 1275 Management. 11 (1), 71–83. https://doi.org/10.1080/21513732.2014.997292
- Maza, M., Adler, K., Ramos, D., Garcia, A. M., Nepf, H., 2017. Velocity and drag evolution from the leading edge of a model Mangrove Forest. Journal of Geophysical Research: Oceans. 122, 9144–9159. doi: 10.1002/2017JC012945
- 1279 Maza, M., Lara, J. L., Losada, I. J., 2019. Experimental analysis of wave attenuation and drag forces in 1280 a realistic fringe Rhizophora Mangrove Forest. Adv. Water Resour. 131:103376. doi: 1281 10.1016/j.advwatres.2019.0 7.006
- Mendez, F. J., Losada, I. J., 2004. An empirical model to estimate the propagation of random breaking and nonbreaking waves over vegetation fields. Coastal Engineering, 51, 103–118. <u>doi:</u> 10.1016/j.coastaleng.2003.11.003
- Mimura, N., Yasuhara, K., Kawagoe, S., Yokoki, H., Kazama, S., 2011. Damage from the Great East Japan Earthquake and Tsunami–a quick report. Mitigation and adaptation strategies for global change, 16 (7), 803–818. https://doi.org/10.1007/s11027-011-9297-7
- Mitchell, W., 2021. Effect of an Idealized Mangrove Forest of Moderate Cross-shore Width on Loads
 Measured on a Sheltered Structure and Comparison with Predicted Forces. MS Thesis, Oregon
 State University.
- Moon, W. C., Chiew, L. Q., Cheong, K. W., Tee, Y. C., Chun, J. B., Lau, T. L., 2019. An experimental study for estimating tsunami wave forces acting on building with seaward and landward macroroughness. Ocean Engineering, 186, 106116. https://doi.org/10.1016/j.oceaneng.2019.106116
- Mori, N., Takahashi, T., Group, T. E. T. J. S., 2012. Nationwide post event survey and analysis of the 2011 Tohoku earthquake tsunami. Coastal Engineering Journal, 54 (1), 1250001–1–1250001–27. https://doi.org/10.1142/S0578563412500015
- Moris, J. P., Kennedy, A. B, Westerink, J. J., 2021. Tsunami wave run-up load reduction inside a building array. Coastal Engineering, 103910. https://doi.org/10.1016/j.coastaleng.2021.103910
- National Academy of Sciences, 1977. Methodology for Calculating Wave Action Effects Associated with Storm Surges. Washington, DC: National Academy of Sciences, 29
- Neelamani, S., Sumalatha, B., 2013. Wave reflection, run-up, run-down and pressures on seawalls defended by an offshore breakwater. Journal of the Indian Institute of Science, 86 (1), 15.
- Neumann. B., Vafeidis. A.T., Zimmermann. J., Nicholls. R.J., 2015. Future Coastal Population Growth and Exposure to Sea-Level Rise and Coastal Flooding A Global Assessment. PLoS ONE 10(3):
- 1306 e0118571. doi: 10.1371/journal.pone.0118571

- NOAA and NHC, 2018. Costliest US tropical cyclones tables updated. NOAA Technical Memorandum NWS NHC-6 3. https://www.nhc.noaa.gov/news/UpdatedCostliest.pdf
- Ohira, W., Honda, K., Nagai, M., Ratanasuwan, A., 2013. Mangrove stilt root morphology modelling for estimating hydraulic drag in tsunami inundation simulation. Trees (Berl.) 27, 141–148. https://doi.org/10.1007/s00468-012-0782-8
- Okal, E. A., Fritz, H. M., Synolakis, C. E., Borrero, J. C., Weiss, R., Lynett, P. J., Titov, V. V., Foteinis, S., Jaffe, B. E., Liu, P. L.–F., 2010. Field survey of the Samoa tsunami of 29 September 2009. Seismological Research Letters, 81 (4), 577–591. https://doi.org/10.1785/gssrl.81.4.577
- Oshnack, M. E., van de Lindt, J., Gupta, R., Cox, D., Aguíñiga, F., 2009. Effectiveness of small onshore seawall in reducing forces induced by Tsunami bore: large scale experimental study. Journal of Disaster Research, 4 (6), 382-390. doi: 10.20965/jdr. 2009.p0382
- Oumeraci, H., 2010. More than 20 Years of Experience Using the Large Wave Flume (GWK)–Selected Research Projects. Die Küste, 77, (77), 179–239. https://hdl.handle.net/20.500.11970/101652
- Ozeren, Y., Wren, D. G., Wu, W., 2014. Experimental investigation of wave attenuation through model and live vegetation. Journal of Waterway, Port, Coastal, and Ocean Engineering. 140:04014019. doi: 10.1061/(asce)ww.1943-5460.0000251
- Palermo, D., Nistor, I., Al–Faesly, T., Cornett, A., 2012. In Impact of tsunami forces on structures: The University of Ottawa experience, Proceedings of the fifth international tsunami symposium, Ispra, Italy, pp 3–5.
- Park, H., Cox, D. T., Lynett, P. J., Wiebe, D. M., Shin, S., 2013. Tsunami inundation modeling in constructed environments: A physical and numerical comparison of free–surface elevation, velocity, and momentum flux. Coastal Engineering, 79, 9–21. https://doi.org/10.1016/j.coastaleng.2013.04.002
- Park, H., Koh, M.–J., Cox, D. T., Alam, M. S., Shin, S., 2021. Experimental study of debris transport driven by a tsunami-like wave: Application for non–uniform density groups and obstacles. Coastal Engineering, 166, 103867. https://doi.org/10.1016/j.coastaleng.2021.103867
- Park, H., Tomiczek, T., Cox, D. T., van de Lindt, J. W., Lomonaco, P., 2017. Experimental modeling of horizontal and vertical wave forces on an elevated coastal structure. Coastal Engineering, 128, 58–74. https://doi.org/10.1016/j.coastaleng.2017.08.001
- Peakall, J., Warburton, J. 1996. Surface tension in small hydraulic river models-the significance of the Weber number. Journal of Hydrology, 199-212. https://www.jstor.org/stable/43944772
- Raby, A., Macabuag, J., Pomonis, A., Wilkinson, S., Rossetto, T., 2015. Implications of the 2011 Great East Japan Tsunami on sea defence design. International Journal of Disaster Risk Reduction, 14, 332–346. https://doi.org/10.1016/j.ijdrr.2015.08.009
- Rahman, S., Akib, S., Khan, M., Shirazi, S., 2014. Experimental study on tsunami risk reduction on coastal building fronted by sea wall. The Scientific World Journal, 2014. https://doi.org/10.1155/2014/729357
- Ramsden, J. D., 1996. Forces on a vertical wall due to long waves, bores, and dry-bed surges. Journal of waterway, port, coastal, and ocean engineering, 122 (3), 134–141. https://ascelibrary.org/doi/pdf/10.1061/(ASCE)0733-950X(1996)122%3A3(134)
- Ranasinghe, R., Turner, I. L., 2006. Shoreline response to submerged structures: A review. Coastal Engineering. 53(1), 65-79. https://doi.org/10.1016/j.coastaleng.2005.08.003
- Reddy, M. M., Sannasiraj, S., Natarajan, R., 2007. Numerical investigation on the dynamics of a vertical wall defenced by an offshore breakwater. Ocean engineering, 34 (5–6), 790–798. https://doi.org/10.1016/j.oceaneng.2006.04.012
- Reese, S., Cousins, W., Power, W., Palmer, N., Tejakusuma, I., Nugrahadi, S., 2007. Tsunami vulnerability of buildings and people in south java- field observations after the July 2006 Java tsunami. Nat. Hazards Earth Syst. Sci. 573–589. www.nat-hazards-earth-syst-sci.net/7/573/2007
- Science for Environmental Policy., 2021. The Solution is in Nature. Future Brief 24. Brief Produced for the European Commission DG Environment. Bristol: Science Communication Unit. https://library.sprep.org/sites/default/files/2021-02/science-environment-policy-solution-nature.pdf
- Shin, S., Bae, I.–R., Lee, J.–I., 2019. Physical Modelling of the Wave Transmission over a Tetrapod Armored Artificial Reef. Journal of Coastal Research, 91 (sp1), 126–130. https://www.jstor.org/stable/26852491

- Silva, R., Losada, I., Losada, M., 2000. Reflection and transmission of tsunami waves by coastal structures. Applied ocean research, 22 (4), 215–223. https://doi.org/10.1016/S0141-1187(00)00012-2
- Sogut, E., Velioglu Sogut, D., Farhadzadeh, A., 2020. Overland Wave Propagation and Load Distribution among Arrays of Elevated Beachfront Structures. Journal of Waterway, Port, Coastal, and Ocean Engineering, 146 (4), 04020016. DOI: 10.1061/(ASCE)WW.1943-5460.0000579
- Sopkin, K. L., Stockdon H. F., Doran K. S., Plant N. G., Morgan K. L., Guy K. K., Smith K. E., 2014. Hurricane Sandy: Observations and Analysis of Coastal Change (No. 2014-1088). US Geological Survey. http://dx.doi.org/10.3133/ofr20141088.
- St–Germain, P., Nistor, I., Townsend, R., 2012. Numerical modeling of the impact with structures of tsunami bores propagating on dry and wet beds using the SPH method. International Journal of Protective Structures, 3 (2), 221–255. https://doi.org/10.1260/2041-4196.3.2.221
- Strusińska-Correia, A., Husrin, S., Oumeraci, H., 2013. Tsunami damping by mangrove forest: a laboratory study using parameterized trees. Natural Hazards Earth System Sciences, 13(2): 483-503. doi:10.5194/nhess-13-483-2013
- Sun, W., Qu, K., Kraatz, S., Deng, B., Jiang, C. B., 2020. Numerical investigation on performance of submerged porous breakwater to mitigate hydrodynamic loads of coastal bridge deck under solitary wave. Ocean Engineering, 213, 107660. https://doi.org/10.1016/j.oceaneng.2020.107660
- Sweet, W.V., Hamlington, B.D., Kopp, R.E., Weaver, C.P., Barnard, P.L., Bekaert, D., Brooks, W., Craghan, M., Dusek, G., Frederikse, T., 2022. Global and Regional Sea Level Rise Scenarios for the United States: Updated Mean Projections and Extreme Water Level Probabilities Along U.S. Coastlines; NOAA Technical Report NOS 01; National Oceanic and Atmospheric Administration: Washington, DC, USA; National Ocean Service: Silver Spring, MD, USA, 2022. https://oceanservice.noaa.gov/hazards/sealevelrise/noaa-nos-techrpt01-global-regional-SLR-scenarios-US.pdf.
- Tanaka, N., Sasaki, Y., Mowjood, M. I. M., Jinadasa, K. B. S. N., Homchuen, S., 2007. Coastal Vegetation Structures and Their Functions in Tsunami Protection: Experience of the Recent Indian Ocean Tsunami. Landscape and Ecological Engineering 3 (1): 33–45. doi:10.1007/s11355-006-0013-9
- Thomas, S., Cox, D., 2012. Influence of finite–length seawalls for tsunami loading on coastal structures.

 Journal of waterway, port, coastal, and ocean engineering, 138 (3), 203–214. <u>DOI:</u>
 1393
 10.1061/(ASCE)WW.1943-5460.0000125
- Ting, C.L., Lin, M.C., Cheng, C.Y., 2004. Porosity effects on non-breaking surface waves over permeable submerged breakwaters. Coastal engineering, 50 (4), 213–224. https://doi.org/10.1016/j.coastaleng.2003.10.003.
- 1397 Tomiczek, T. Cox, D. Lomonaco, P. Wargula, A. Kennedy, A. Lynett, P. Maddux, T., 2021 Transient 1398 Wave Transformation through Reduced-Scale Physical Model of Mangrove Forests of Moderate 1399 Cross-Shore Width. in Experimental Investigation of Wave, Surge, and Tsunami Transformation 1400 Reduced Over Natural Shorelines: Scale Physical Model. DesignSafe-1401 CI. https://doi.org/10.17603/ds2-j0j1-5827
- Tomiczek, T., O'Donnell, K., Furman, K., Webbmartin, B., Scyphers, S., 2020b. Rapid damage assessments of shorelines and structures in the Florida Keys after hurricane Irma. Nat. Hazards Rev. 21:05019006. DOI: 10.1061/(ASCE)NH.1527-6996.0000349
- Tomiczek, T., Prasetyo, A., Mori, N., Yasuda, T., Kennedy, A., 2016. Physical modelling of tsunami onshore propagation, peak pressures, and shielding effects in an urban building array. Coastal Engineering, 117, 97–112. https://doi.org/10.1016/j.coastaleng.2016.07.003
- Tomiczek, T., Wargula, A., Jendrysik, M., Goodwin, S., Kennedy, A., Lynett, P., Lomonaco, P., Cox,
 D., 2019. Physical Model Investigation of Parcel–Scale Effects of Mangroves on Wave
 Transformation and Force Reduction in the Built Environment. Coastal Structures, 998–1007.
 https://doi.org/10.18451/978-3-939230-64-9_100
- Tomiczek, T., Wargula, A., Lomónaco, P., Goodwin, S., Cox, D., Kennedy, A., Lynett, P., 2020a.

 Physical model investigation of mid–scale mangrove effects on flow hydrodynamics and pressures
- 1414 and loads in the built environment. Coastal Engineering, 162, 103791.
- 1415 <u>https://doi.org/10.1016/j.coastaleng.2020.103791</u>

- Twu, S.W., Liu, C.C., Hsu, W.H., 2001. Wave damping characteristics of deeply submerged breakwaters. Journal of Waterway, Port, Coastal and Ocean Engineering, 127(2): 97–105. https://doi.org/10.1061/(ASCE)0733-950X(2001)127:2(97)
- UNDRR, 2021. Words Into Action: Engaging for Resilience in Support of the Sendai Framework for
 Disaster Risk Reduction 2015 2030, United Nations Office for Disaster Risk Reduction. Bangkok:
 Regional Office for Asia and the Pacific.
- 1422 UNEP, 2005. Maldives post-tsunami environmental assessment. UNEP, Nairobi, Kenya, p 19.
- Winter, A. O., Alam, M. S., Shekhar, K., Motley, M. R., Eberhard, M. O., Barbosa, A. R., Lomonaco,
 P., Arduino, P., Cox, D. T., 2020. Tsunami-like wave forces on an elevated coastal structure: Effects
 of flow shielding and channeling. Journal of Waterway, Port, Coastal, and Ocean Engineering, 146
 (4), 04020021. DOI: 10.1061/(ASCE)WW.1943-5460.0000581
- Wu, W. C., Cox, D. T., 2015. Effects of wave steepness and relative water depth on wave attenuation by emergent vegetation. Estuarine, Coastal and Shelf Science. 164, 443–450. <u>doi:</u> 10.1016/j.ecss.2015.08.009
- Wu, W. C., Cox, D. T., 2016. Effects of vertical variation in vegetation density on wave attenuation.

 Journal of Waterway, Port, Coastal, and Ocean Engineering. 142:04015020. doi: 10.1061/(asce)ww.1943-5460.000 0326
- Wu, Y. T., Hsiao, S.-C., 2013. Propagation of solitary waves over a submerged permeable breakwater.

 Coastal Engineering, 81, 1-18. https://doi.org/10.1016/j.coastaleng.2013.06.005
- Wüthrich, D., Pfister, M., Nistor, I., Schleiss, A. J., 2018. Experimental study on forces exerted on buildings with openings due to extreme hydrodynamic events. Coastal Engineering, 140, 72–86.
 https://doi.org/10.1016/j.coastaleng.2018.06.002
- 1438 Xu, Z., Melville, B., Whittaker, C., Nandasena, N., Shamseldin, A., 2021. Mitigation of tsunami bore 1439 impact on a vertical wall behind a barrier. Coastal Engineering, 164, 103833. 1440 https://doi.org/10.1016/j.coastaleng.2020.103833